The Astrophysical Journal, 820:34 (20pp), 2016 March 20 doi:10.3847/0004-637X/820/1/34
© 2016. The American Astronomical Society. All rights reserved.

EN ROUTE TO DESTRUCTION: THE EVOLUTION IN COMPOSITION OF ICES IN COMET D/2012 S1 (ISON) BETWEEN 1.2 AND 0.34 AU FROM THE SUN AS REVEALED AT INFRARED WAVELENGTHS*

M. A. DiSanti[1,2,9], B. P. Bonev[1,3,9], E. L. Gibb[1,4,9], L. Paganini[1,3,10], G. L. Villanueva[1,3,10], M. J. Mumma[1,2,10], J. V. Keane[5,10], G. A. Blake[1,6], N. Dello Russo[7,9], K. J. Meech[5], R. J. Vervack, Jr.[7,9], and A. J. McKay[8,9]
[1] Goddard Center for Astrobiology, NASA Goddard Space Flight Center, Greenbelt, MD, USA; michael.a.disanti@nasa.gov
[2] Solar System Exploration Division, Code 690, NASA Goddard Space Flight Center, Greenbelt, MD, USA
[3] Department of Physics, The Catholic University of America, Washington, DC, USA
[4] Department of Physics and Astronomy, University of Missouri–St. Louis, Saint Louis, MO, USA
[5] Institute for Astronomy, University of Hawaii at Manoa, Honolulu, HI, USA
[6] Division of Geological and Planetary Sciences, California Institute of Technology, Pasadena, CA, USA
[7] The Johns Hopkins University Applied Physics Laboratory, Laurel, MD 20723-6099, USA
[8] University of Texas–Austin/McDonald Observatory, Austin, TX, USA
Received 2015 May 5; accepted 2015 December 14; published 2016 March 16

ABSTRACT

We report production rates for H_2O and eight trace molecules (CO, C_2H_6, CH_4, CH_3OH, NH_3, H_2CO, HCN, C_2H_2) in the dynamically new, Sun-grazing Comet C/2012 S1 (ISON), using high-resolution spectroscopy at Keck II and the NASA IRTF on 10 pre-perihelion dates encompassing heliocentric distances $R_h = 1.21$–0.34 AU. Measured water production rates spanned two orders of magnitude, consistent with a long-term heliocentric power law $Q(H_2O) \propto R_h^{(-3.1\pm0.1)}$. Abundance ratios for CO, C_2H_6, and CH_4 with respect to H_2O remained constant with R_h and below their corresponding mean values measured among a dominant sample of Oort Cloud comets. CH_3OH was also depleted for $R_h > 0.5$ AU, but was closer to its mean value for $R_h \leq 0.5$ AU. The remaining four molecules exhibited higher abundance ratios within 0.5 AU: for $R_h > 0.8$ AU, NH_3 and C_2H_2 were consistent with their mean values while H_2CO and HCN were depleted. For $R_h < 0.5$ AU, all four were enriched, with NH_3, H_2CO, and HCN increasing most. Spatial profiles of gas emission in ISON consistently peaked sunward of the dust continuum, which was asymmetric antisunward and remained singly peaked for all observations. NH_3 within 0.5 AU showed a broad spatial distribution, possibly indicating its release in the coma provided that optical depth effects were unimportant. The column abundance ratio NH_2/H_2O at 0.83 AU was close to the "typical" NH/OH from optical wavelengths, but was higher within 0.5 AU. Establishing its production rate and testing its parentage (e.g., NH_3) require modeling of coma outflow.

Key words: astrochemistry – comets: general – comets: individual (C/2012 S1 (ISON)) – molecular processes – Oort Cloud

1. COMET D/2012 S1 (ISON): A UNIQUE OBSERVATIONAL OPPORTUNITY

Comets contain the most primitive remnant material from the formation of our solar system. The abundances of their ices encode information pertaining to conditions in the formative epoch, and building a taxonomy of comets based on their volatile composition reflects differences in physical and/or chemical conditions in the nascent environment (Mumma & Charnley 2011; Bockelée-Morvan et al. 2004, and references therein). Taxonomic studies reveal a range of compositions among comets. However, owing to observing circumstances and limited availability of time on large telescopes, for the most part observations of individual comets represent mere snapshots of their activity rather than studies over a range of heliocentric distances (R_h). They are also typically conducted at R_h approaching or often exceeding 1 AU—the ability to conduct measurements in sufficiently bright comets over a range in R_h and to small heliocentric distances (particularly within 0.5 AU) is very rare.

One such opportunity serendipitously presented itself with the early discovery of Comet C/2012 S1 (ISON) on 2012 September 21 (at $R_h = 6.29$ AU) by the International Scientific Optical Network telescope in Russia (Nevski & Novichonok 2012). ISON was soon thereafter recognized as a Sun-grazing comet, with perihelion at distance $q = 0.0124$ AU on 2013 November 28. Moreover, its original semimajor axis ($1/a_0 = -1.1 \times 10^{-5}$ AU^{-1}; Nakano Note 2587) classified ISON as a dynamically new comet from the Oort Cloud.

The rare occurrence of a Sun-grazing comet entering the inner solar system for the first time since being emplaced in the Oort Cloud afforded the opportunity to search for changes in composition, as its primordial surface was replaced by interior material that (presumably) was better shielded over cosmogonic time. This unique combination (dynamically new and Sun-grazing; Knight & Schleicher 2015)[11] provided compelling incentive for study, with more than a year available to prepare a worldwide ground- and space-based observing campaign for serial measurements of gas and dust, including the observations at the W. M. Keck and NASA Infrared Telescope Facility

* This paper includes data collected at the W. M. Keck Observatory, Maunakea, HI, USA, operated as a scientific partnership among Caltech, UCLA, and NASA, and made possible by the generous financial support of the W. M. Keck Foundation.
[9] Visiting astronomer at the Infrared Telescope Facility, which is operated by the University of Hawaii under contract NNH14CK55B with the National Aeronautics and Space Administration.
[10] Visiting astronomer at the W. M. Keck Observatory, Maunakea, HI, USA.
[11] In addition to the introduction of Knight & Schleicher (2015), see the 2013 July blog post, "How Unique Is Comet ISON?," by M. M. Knight (http://isoncampaign.org/mmk/how-unique-is-ISON).

(IRTF) observatories reported here. All ISON data obtained with NASA-allocated time at Keck and all data from the IRTF were immediately placed in the public domain.

In this paper we use high-resolution spectroscopy of ISON to establish the evolution of pre-perihelion production rates for water (Section 4.1) and production rates and abundance ratios relative to H_2O for eight trace volatiles (CO, CH_4, C_2H_6, CH_3OH, H_2CO, C_2H_2, HCN, and NH_3) to well within 1 AU of the Sun, and we also report column densities for NH_2 and their ratios relative to H_2O at three heliocentric distances (Section 4.2). We place Comet ISON in taxonomic context and discuss possible implications for the overall composition of its ices and their evolution with decreasing R_h under conditions of steadily and dramatically increasing solar irradiation. We examine the measured spatial distributions (Section 5) of the gas and dust to assess the nature of release, for example, directly from the nucleus versus from one or more distributed sources in the coma.

2. NEAR-IR SPECTRAL OBSERVATIONS OF COMET ISON AT KECK II AND THE NASA IRTF

We report results from long-slit high-resolution ($\lambda/\Delta\lambda \approx$ 25,000) spectra of Comet ISON on 10 pre-perihelion UT dates between 2013 October 22 and November 22 (R_h = 1.213–0.344 AU) and spanning wavelengths 2.83–5.0 μm. We include observations from four dates[12] using the powerful cross-dispersed spectrograph (NIRSPEC; McLean et al. 1998, 2000) at Keck II and from six dates using the Cryogenic Echelle Spectrometer (CSHELL; Tokunaga et al. 1990; Greene et al. 1993) at the IRTF. Additional NASA-allocated NIRSPEC observations on October 26 and 28 and CSHELL observations on November 19 and 20 are reported in a separate paper (Dello Russo et al. 2016; settings from November 19 appropriate to our serial study are included here). Two other scheduled NASA-allocated NIRSPEC dates (November 11 and 12) were lost completely to weather. Of 10 CSHELL dates scheduled pre-perihelion for ISON, three were lost to weather (November 10, 14, and 21), and although intermittent cirrus was present during the November 20 observations, reliable production rates and abundances were obtained (Dello Russo et al. 2016). Studies of water excitation in the coma of Comet ISON on two CSHELL dates included in this study (November 17 and 22) are published (Bonev et al. 2014, hereafter Paper 1). Owing to the complete disruption of Comet ISON near perihelion, scheduled post-perihelion NASA-allocated time (six dates with CSHELL, and three dates with NIRSPEC) was canceled or redirected to other targets.

Table 1 provides a log of the observations and a list of targeted species that are addressed here. On November 16, 17, and 22, intersetting gaps in UT in Table 1 resulted from time dedicated to a deep search for deuterated water (HDO), the results of which are presented separately (Gibb et al. 2016). The paucity of settings on November 18 resulted from the onset of thickening cirrus around 19:00 UT that prevented additional observations for the remainder of that day.

Both NIRSPEC and CSHELL observations used the standard ABBA nod sequence with A and B beams present in the slit, separated by 12 and 15 arcsec, respectively, and placed at symmetric positions with respect to its midpoint (e.g., Figures 1(A)–(C) in DiSanti et al. 2006 illustrate the placement of beams). The methodology used for processing the spectra is detailed elsewhere (Bonev 2005; DiSanti et al. 2006; Villanueva et al. 2009; Radeva et al. 2010) and so is not repeated, except for aspects pertaining uniquely to the Comet ISON observations addressed here. Instead, we present (in Section 3.1) a new approach we developed to accurately model the spectra for arriving at optimal molecular production rates (as detailed in Appendices A.1 and A.2).

The NIRSPEC observations were conducted during the final 1–1.5 hr of the night, and on all dates active or offset guiding was employed—any small drift of the comet during acquisition of spectra was generally within the atmospheric seeing (typically 0.5–0.9 arcsec). On each date, prior to acquiring the comet an IR flux standard star was observed to establish absolute intensities of cometary continuum and line emissions. The cross-dispersing capability of NIRSPEC permitted sampling multiple trace volatiles simultaneously with H_2O (Table 1).

The CSHELL observations of Comet ISON were conducted entirely after sunrise, and spectra were obtained until the minimum allowable solar elongation angle at the IRTF (20°) was reached, on November 22.[13] However, the CSHELL CCD guider could not be used; instead, ISON was maintained at or near the nominal beam positions by frequent imaging in the infrared using the CSHELL open (30 × 30 arcsec) aperture—typically every 3–5 minutes based on the cadence of individual ABBA spectral sequences. This allowed recording the comet's drift during acquisition of spectra, repositioning it in the slit at the nominal (A-beam) position, and making small adjustments to the non-sidereal tracking rates as needed to correct for systematic (i.e., repeated directional) drift on the array (e.g., see Paper 1 and DiSanti et al. 2006 for discussions regarding daytime observing of non-sidereal targets with CSHELL). Over the course of an ABBA spectral sequence this drift was at most 2–3 arcsec (but was generally much less) and was predominantly along the slit. This allowed for accurate spatial registration of individual A and B beams during processing of the data, and as a result nearly all spectra obtained are included in our analysis.

Typical daytime seeing varied between ~0.8 and 1.9 arcsec and was estimated using the point-spread function (PSF) of a field star near the comet immediately prior to its acquisition, and also through spatially extended spectra of IR flux standards observed prior to and/or following the comet observations. On each date, corrections to the telescope focus were implemented throughout the observing period, based on the ambient (i.e., IRTF dome) temperature. Additionally, occasional checks were made on field stars to ensure that optimal focus was maintained.

Because CSHELL provides limited spectral grasp (i.e., spectral coverage within a setting; see Table 1, note c), settings must be chosen judiciously to optimize sampling of molecular emission and thereby to minimize systematic uncertainties. In most cases, trace species were measured simultaneously with water, targeting emissions adjacent in frequency to lines of H_2O and/or OH prompt emission (OH^*), the latter being a proxy for H_2O in the cometary atmosphere (e.g., see Bonev 2005; Bonev et al. 2006). Rotational temperatures (T_{rot}; see Section 3.2.1) are required to establish accurate molecular

[12] October 22 was University of Hawaii time, October 24 and 25 were NASA time, and November 7 was Caltech time.

[13] On November 22, ISON was nearly due west of the Sun, and as a consequence, to avoid exposure of the primary to direct sunlight, it was necessary to vignette (occult) the telescope primary by an estimated 50% for the first ~2 hr of observing. This attenuated the signal in the first three settings reported here; accordingly, we have applied a systematic correction (and associated uncertainty; see Bonev et al. 2014 and Gibb et al. 2016).

Table 1
Log of IR Spectral Observations of D/2012 S1 (ISON)

NIRSPEC[a]

2013 UT Date	Setting ID[b]	$\Delta\nu$[c] (cm^{-1})	Γ[d] 10^{-18} W m^{-2} $(cm^{-1})^{-1}$/(ADU s^{-1})	UT Start-End	R_h (AU)	Δ (AU)	$d\Delta/dt$ (km s^{-1})	Molecule(s) (order)[e]	T_{int}[f] [sec]	Slit PA (deg)[g]
Oct 22	**HR1552**			11:38–11:45						
	MWA	2161 – 2127	0.6490	15:00–15:11	1.213	1.502	−52.08	CO, H_2O (16)	360	290
	KL1	3400 – 3353	1.172	15:17–15:57	1.212	1.502	−52.06	H_2O (26, 27)	1440	290
		3529 – 3482	1.200							
		3400 – 3353	1.172					NH_3 (26)		(290)
		3009 – 2968	0.8227					C_2H_6 (23)		
		2878 – 2839	0.8281					CH_3OH (22, 23)		
		3009 – 2968	0.8227							
Oct 24	**HR1552**			13:17–13:33						
	MWA	2161 – 2127	0.6490	14:47–14:51	1.168	1.443	−51.70	CO, H_2O (16)	120	293
	KL1	3400 – 3353	1.137	15:01–15:57	1.168	1.442	−51.65	H_2O (26, 27)	2160	293
		3529 – 3482	1.218							
		3400 – 3353	1.137					NH_3 (26)		(293)
		3009 – 2968	0.8000					C_2H_6 (23)		
		2878 – 2839	0.8040					CH_3OH (22, 23)		
		3009 – 2968	0.8000							
Oct 25	**HR1552**			13:10–13:19						
	KL2	3471 – 3419	0.7982	14:29–16:01	1.146	1.413	−51.41	H_2O (26)	3360	293
		3339 – 3288	0.8000					HCN, C_2H_2, NH_3, OH^* (25)		(293)
		3073 – 3027	0.6496					CH_4, OH^* (23)		
		2807 – 2764	0.5787					H_2CO, OH^* (21)		
Nov 7	**HR4386**			14:25–14:28						
	KL2	3471 – 3419	1.316	14:37–16:05	0.829	1.056	−42.08	H_2O (26)	720	256
		3339 – 3288	1.220					HCN, C_2H_2, NH_3, OH^*, NH_2 (25)		(294)
		3205 – 3158	1.086					OH^* (24)		
		3073 – 3027	0.9894					CH_4, OH^* (23)		
		2940 – 2896	0.9942					C_2H_6 (22)		
		2807 – 2764	0.9344					H_2CO, OH^* (21)		

CSHELL[a]

2013 UT Date	Setting ID[b]	ν_{cent}(cm^{-1})[c]	Γ[d] 10^{-18} W m^{-2} $(cm^{-1})^{-1}$/(ADU s^{-1})	UT Start-End	R_h (AU)	Δ (AU)	$d\Delta/dt$ (km s^{-1})	Molecule(s)[e]	T_{int}[f] [sec]	Slit PA (deg)[g]
Nov 15	H2O_3A	3452.6	61.50	18:35–19:07	0.596	0.896	−23.68	H_2O	960	270
	CO_K	2152.9	20.38	20:11–20:28	0.594	0.895	−23.33	CO, H_2O	360	(291)
	CH4_E	3041.1	38.78	20:56–21:44	0.594	0.895	−23.06	CH_4, OH^*	1440	
	C2H6_A	2984.3	40.13	21:51–22:08	0.592	0.895	−22.90	C_2H_6, CH_3OH	960	
	HR5107			22:28–22:53						
Nov 16	**HR4357**			15:36–16:03						
	H2O_3A	3452.6	60.15	16:57–17:56	0.566	0.884	−20.58	H_2O	1200	270
	CO_K	2152.9	17.83	21:36–22:12	0.560	0.882	−19.46	CO, H_2O	840	(290)
Nov 17	**HR4357**			16:05–16:38						
	H2O_3A	3452.6	56.47	17:44–18:08	0.533	0.874	−16.71	H_2O	1440	289
	CO_K	2152.9	18.61	22:27–22:46	0.527	0.872	−15.45	CO, H_2O	480	(289)
	H2O_3A	3452.6	56.47	22:50–23:34	0.526	0.872	−15.29	H_2O	1440	
	C2H6_A	2984.3	34.00	23:38–00:04	0.525	0.871	−15.16	C_2H_6, CH_3OH	720	
	HR5235			00:20–00:30						
Nov 18	**HR4357**			15:41–15:58						
	CH3OH_A	2842.1	28.87	16:28–17:05	0.501	0.866	−12.85	CH_3OH, OH^*	960	270
	H2O_3A	3452.6	60.99	17:09–18:11	0.500	0.865	−12.63	H_2O	1440	(288)
Nov 19	H2O_3B	3514.5	45.22	17:00–17:20	0.466	0.860	−8.22	H_2O	480	270
	C2H6_A	2984.3	36.62	17:25–17:40	0.466	0.859	−8.12	C_2H_6, CH_3OH	480	(287)
	H2O_3A	3452.4	61.57	17:43–18:02	0.465	0.859	−7.98	H_2O	640	

Table 1
(Continued)

CSHELL[a]										
2013 UT Date	Setting ID[b]	ν_{cent}(cm^{-1})[c]	Γ[d] 10^{-18} W m^{-2} $(cm^{-1})^{-1}$/(ADU s^{-1})	UT Start-End	R_h (AU)	Δ (AU)	dΔ/dt (km s^{-1})	Molecule(s)[e]	T_{int}[f] [sec]	Slit PA (deg)[g]
	HCN_A	3302.6	78.59	18:06–18:58	0.464	0.859	−7.82	HCN, C_2H_2, OH, NH_2	1920	
	H2O_3C	3379.2	50.98	19:05–19:45	0.463	0.859	−7.52	H_2O, OH, NH_3	1440	
	H2CO_A	2783.5	34.28	19:55–20:40	0.462	0.859	−7.30	H_2CO, OH*	1440	
	H2O_5A	2003.9	21.98	22:08–22:54	0.458	0.859	−6.61	H_2O	1200	
	H2O_3B	3514.5	45.22	23:02–23:30	0.457	0.858	−6.43	H_2O	320	
	HR5793			22:34–22:59						
Nov 22	C2H6_A	2984.3	41.37	17:17–17:37	0.353	0.860	8.49	C_2H_6, CH_3OH	720	270
	H2O_3A	3452.4	64.85	17:43–18:01	0.353	0.860	8.63	H_2O	720	(281)
	HCN_A	3302.5	80.38	18:02–18:15	0.352	0.860	8.74	HCN, C_2H_2, OH, NH_2	480	
	H2O_3A	3452.4	64.85	19:25–19:36	0.350	0.860	9.23	H_2O	480	
	CO_K	2152.9	21.33	22:23–22:36	0.345	0.861	10.36	CO, H_2O	360	
	H2O_3A	3452.4	64.85	22:42–22:53	0.345	0.861	10.46	H_2O	480	
	H2O_3C	3379.2	51.49	22:57–23:14	0.344	0.861	10.58	H_2O, OH, NH_3	720	
	HR6629			23:32–00:06						

Notes.
[a] The slit dimensions for NIRSPEC (CSHELL) were 0.43 (1.0) arcsec width by 24 (30) arcsec length, and the spatial scale was 0.198 (0.20) arcsec $pixel^{-1}$.
[b] Spectral settings were chosen to optimize the sampling of molecular composition. IR flux standard stars observed on each date are identified in bold and were measured in all settings used for Comet ISON.
[c] Each NIRSPEC setting included multiple echelle orders simultaneously, and $\Delta\nu$ is the approximate frequency range covered within each order. With CSHELL, the central wavenumber for each setting (ν_{cent}) is listed, and the spectral range encompassed by each was approximately $2.3 \times 10^{-3} \times \nu_{cent}$.
[d] Flux calibration factor. On all dates we estimate ±5% uncertainty (1σ) in Γ.
[e] Encompassed molecules/radicals that are addressed in this paper. For NIRSPEC the echelle order in which emissions occur is also listed.
[f] Total on-source integration time.
[g] The first entry for each UT date is slit position angle on the sky. The second entry (in parentheses) is the PA of the extended heliocentric radius vector (i.e., the projected Sun–comet direction) for ISON. With NIRSPEC the slit PA was along the projected Sun–comet direction on all dates, while with CSHELL it was oriented east–west (PA = 270°) on all dates except November 17, when it was along the Sun–comet direction (PA = 289°; see Paper 1).

production rates—we included on all dates a CSHELL setting (H2O_3A; see Tables 1 and 2) that encompassed multiple strong water lines that together spanned a sufficient range of rotational energies. This setting was also used for the spatially resolved studies of November 17 (R_h = 0.53 AU) and 22 (R_h = 0.35 AU) (Paper 1) and of November 19 (R_h = 0.46 AU; Dello Russo et al. 2016).

3. METHODOLOGY FOR ANALYZING SPECTRAL DATA

3.1. Iterative Approach to Establishing Telluric and Cometary Spectral Components

As discussed in Paper 1, the observed spectra encode signatures from two important components: (1) time- and frequency-dependent extinction due to absorbing species in the telluric atmosphere, and (2) emission from gaseous species in the cometary coma. Accurate treatment of the data requires quantifying both components—the first through a modeled transmittance function using the LBLRTM radiative transfer code (Clough et al. 2005) with updated line lists and strengths (Villanueva et al. 2011), the second through application of our line-by-line quantum band models of molecular fluorescent emission. Publications for the molecular fluorescence models used here are cited in Section 3.1 of DiSanti et al. (2014) and Section 3.1 of Paganini et al. (2014). As part of the fitting process, models of both telluric extinction and cometary emission are convolved to the spectral resolving power of the data. An example and a description of our iterative approach are presented in Appendix A.1.

3.2. Measuring Rotational Temperatures and Molecular Production Rates

Representative examples of our modeled NIRSPEC and CSHELL spectra are shown in Figures 1 and 2, respectively. These demonstrate the dramatic increase in brightness experienced by Comet ISON between 2013 October 22 (R_h = 1.2 AU) and November 22 (R_h = 0.35 AU). For example, the observed 4.65 μm continuum intensity on November 22 (Figure 2(d)) increased by a factor of ~7 compared with that on November 15 (R_h = 0.60 AU, Figure 2(b)) owing to the smaller heliocentric distance (Table 1) and therefore higher dust temperature. Despite the lower line-to-continuum contrast on November 22, emission-line intensities were nonetheless much higher than on November 15. This also demonstrates the need for accurate modeling of the telluric transmittance function (spectral component 1 in Section 3.1).

3.2.1. Rotational Temperatures

Obtaining accurate molecular production rates requires knowledge of excitation conditions in the coma. This establishes the fractional strength of each ro-vibrational band encompassed by the lines observed and is expressed through a rotational temperature (T_{rot}). On all dates, T_{rot} was measured by comparing the relative intensities of simultaneously observed H_2O lines after

correcting each for telluric transmittance at its Doppler-shifted frequency. For ISON, the NIRSPEC data lacked sufficient signal-to-noise ratio to permit measuring $T_{\rm rot}$ for species other than H_2O, and CSHELL did not sample a sufficient range in rotational energy with adequate signal-to-noise ratio except in the H2O_3A setting. Consequently, on each date we assumed that the value of $T_{\rm rot}$ measured for H_2O applied to all molecules.

This assumption has been validated in comets in which we measured $T_{\rm rot}$ for multiple species (including H_2O; e.g., C/2007 N3 Lulin; see Gibb et al. 2012), independent of observational circumstances (i.e., heliocentric and geocentric distance). In general, we observe common $T_{\rm rot}$ among different species in a given comet, for comets having very different gas production rates. $T_{\rm rot}$ primarily depends on local densities and therefore collision rates in the coma—these in turn are most strongly dependent on gas production and are less dependent on geometry. Even for the relatively few cases of differing $T_{\rm rot}$ among molecules (e.g., 86 K for H_2O, and 76 K for HCN in C/2004 Q2 Machholz; Bonev et al. 2009), the values agree within their 1σ uncertainties. This also holds for species with greatly differing photodissociation lifetimes. For example, C/2002 T7 (LINEAR) showed $T_{\rm rot}$ consistent with 100 K at $R_h = 0.67$–0.71 AU, for both H_2O and H_2CO (DiSanti et al. 2006; Anderson 2010) even though the lifetimes of these two molecules differ by more than an order of magnitude (see Section 5.2.3, and note c of Table 2). We also find molecular mixing *ratios* (i.e., abundances relative to H_2O) to be relatively insensitive to the exact (common) value of $T_{\rm rot}$.

Table 2 lists values of $T_{\rm rot}$ used in our analysis, either as measured or adopted (the latter are shown in parentheses). Our values are based on apertures centered on the nucleus (i.e., on the location of peak H_2O emission) and are thus heavily weighted toward the inner coma. They are consistent with the measured values of $T_{\rm rot}$ averaged over this "nucleus-centered" spatial region (see below) from the H2O_3A setting on November 17 and 22 (Paper 1) and on November 19 (Dello Russo et al. 2016).

3.2.2. Production Rates

We calculated "nucleus-centered" production rates ($Q_{\rm nc}$) using our well-established formalism (e.g., see Bonev 2005; Villanueva et al. 2011, and Section 3.2 of DiSanti et al. 2014 for additional details). These are established for each measured line and are based on its flux $F_{\rm line}$ (W m^{-2}, corrected for telluric transmittance), the molecular photodissociation lifetime (τ_1, s), and line g-factor (g_1, W molecule^{-1}) at the measured (or adopted) value of $T_{\rm rot}$ (both τ_1 and g_1 correspond to values at $R_h = 1$ AU):

$$Q_{\rm nc,line} = \frac{4\pi\Delta^2}{\tau_1 f(x)} \frac{F_{\rm line}}{g_{1,\rm line}}. \quad (1)$$

In our calculations we adopt a gas outflow speed $v_{\rm gas} = 800\, R_h^{-0.5}$ m s^{-1}, based on velocity-resolved observations of several moderately bright comets at radio wavelengths (Biver et al. 2006, 2011; Agúndez et al. 2014; Cordiner et al. 2014). The parameter $f(x)$ represents the fraction of all molecules in the coma contained in the beam, assuming release solely from the nucleus and uniform gas outflow in the coma—$f(x)$ was originally formulated for a circular aperture (Yamamoto 1982) and later revised for square pixels (see Appendix in Hoban et al. 1991). This geometric factor includes molecular photodissociation, expressed through a scale length $\Lambda = v_{\rm gas}(R_h = 1\ {\rm AU}) \times \tau_1 \times R_h^{1.5}$. We list $f(x)$ by species in Table 2 for our nucleus-centered beam and refer to this as fx_01, as it enters into the expression for the corresponding column density (also tabulated; see Table 2, note e).

In practice, for each molecule $Q_{\rm nc}$ represents the mean of its nucleus-centered production rates, which are proportional to F/g for each measured individual line—or group of lines within one or more adjacent resolution elements—weighting each by the inverse square of its stochastic error. Converting to total (or global) production rate ($Q_{\rm tot}$) requires multiplying $Q_{\rm nc}$ by a "growth factor" (GF in Table 2), obtained through application of the "Q-curve" formalism to spatial profiles of molecular emission. Figure 3 shows representative emission profiles for Comet ISON (see Appendix A.3 for details of the application).

4. PRODUCTION RATES AND MOLECULAR ABUNDANCES IN COMET ISON

4.1. Evolution of Water Production in Comet ISON

Figure 4 shows 32 measurements of $Q_{\rm tot}$ for water using lines of H_2O itself (diamonds) or OH prompt emission (OH*, blue circles), with error bars on all points representing $\pm 1\sigma$ uncertainties. The NIRSPEC measurements were obtained simultaneously (i.e., within a single setting on each date) and represent signal averaged over 1–1.5 hr of clock time—to improve their visibility, we show the five individual measurements from November 7 separated in time. The CSHELL measurements are temporally distinct as shown, with a typical resolution of 0.5–1 hr of clock time.

Inspection of Figure 4 suggests that the dominant variation in water production in ISON for $R_h \geqslant 0.5$ AU (i.e., through November 18) was day-to-day. Most dramatic was a decrease from November 15 to 16 by a factor of approximately 2.5, followed by an approximately twofold increase on November 17. On November 19 and 22, we observed significant variations on timescales of hours. On November 19, we identified three distinct regimes of water production, based on groupings of points in Figure 4, and spanning the following UT intervals (taken from Table 1): (1) UT 17:00–19:45, (2) UT 19:55–20:40, and (3) UT 22:08–23:30. On November 22, we identified two such intervals: (1) UT 17:43–18:01 and (2) UT 19:25–23:14. In Table 2, measurements of H_2O are grouped with simultaneous (or contemporaneous) measurements of trace volatiles (see Section 4.2).

When combined with coma outflow models, the (seeing-limited) spatial resolution obtained with NIRSPEC and CSHELL meant that most molecules transited the slit aperture and were replaced by newly released material approximately every 10 minutes for the CSHELL "nucleus-centered" beam. As a consequence, our measurements provide excellent temporal resolution for the evolution of activity of Comet ISON. Comparisons with other measurements of water production in ISON are presented in Section 4.1.2.

The spatial coverage of our observations ($\pm$900–950 km from the nucleus for the nucleus-centered aperture) was much shorter than the photodissociation scale length of H_2O, even on November 22 ($\sim 1.4 \times 10^4$ km); thus, relatively few molecules of H_2O (and most other molecules we measure) decayed within the column encompassed by our nucleus-centered field of view assuming their release directly from the nucleus. In contrast, the slit dimensions were comparable to (or somewhat greater

than) the scale lengths of H_2CO and NH_3. This is discussed in greater detail in Section 5.2.3.

4.1.1. Heliocentric Fits to Water Production

Fitting the dependence of $Q(H_2O)$ on heliocentric distance allows comparison with the canonical "insolation-limited" R_h^{-2} dependence expected for gas production governed by incident solar flux. Inspection of Figure 4 reveals that between October 22 and November 22, $Q(H_2O)$ spanned two orders of magnitude while R_h decreased by a factor of 3.4; thus, a heliocentric dependence steeper than R_h^{-2} is evident.

To quantify this, we performed linear least-squares weighted fits to the water measurements. Including all 32 measurements resulted in a heliocentric dependence $Q(H_2O) \propto R_h^{(-3.28\pm0.18)}$, much steeper than the insolation-limited case. We also performed a fit excluding points associated with periods of enhanced activity, one around November 12–14 (Biver et al. 2013; Crovisier et al. 2013; Opitom et al. 2013b; Agúndez et al. 2014) and one around November 19 (Opitom et al. 2013a); we refer to these periods as "Events 1 and 2" (see Section 4.1.2). Accordingly, we omit the three points from November 15, the point from interval 2 and the two points from interval 3 on November 19, and the point from interval 1 on November 22; these seven points are enclosed in rectangular boxes in Figure 4. Our fit to the 25 remaining points, represented by the dot-dashed line, corresponds to $Q(H_2O)\ \alpha R_h^{-(3.10\pm0.09)}$, still much steeper than insolation limited. We take this fit to be our best measure of the long-term heliocentric dependence of water production over the range 1.2–0.34 AU. Our two fits agree within their 1σ confidence limits.

4.1.2. Comparisons with Other Measurements of Water Production in Comet ISON

ISON was clearly in the process of shedding substantial amounts of material, particularly within $R_h \sim 0.7$ AU. This was exemplified by two periods of enhanced water production (i.e., outbursts; following the terminology of Sekanina & Kracht 2014, we refer to these as "Events"). "Event 1" occurred in the range $R_h = 0.7$–0.6 AU, shortly prior to our November 15 observations, and the decrease in activity we observed from then to November 16 likely reflected its cessation. The report of lengthening "coma wings" in optical images from November 14 and 16 (Boehnhardt et al. 2013) provided further evidence of the dynamic evolution in activity experienced by Comet ISON around that time.

Our higher values for $Q(H_2O)$ observed late on November 19 and early on November 22 bracket another period of increased activity ("Event 2," around heliocentric distance 0.4 AU). (In addition to the compilation of $Q(H_2O)$ by Sekanina and Kracht, an increase in the production rate of sodium [by a factor >3] around the time of "Event 2," between UT November 19.5 and 20.5 [prior to and following our November 19 observations, respectively], was reported from optical spectra [Schmidt et al. 2015].) Substantial variations in activity were also recognized from *Solar and Heliospheric Observatory* (*SOHO*) observations of the highly extended H Lyα coma, from which H_2O production rates as high as (1.6–2) $\times 10^{30}$ molecules s^{-1} were reported for the period November 21–23 (Combi et al. 2014). The *SOHO* observations are highly complementary to our study: compared with our observations, they provide excellent temporal coverage, however, with lower temporal resolution (e.g., days) owing to their much larger field of view (i.e., effective beam size). Such a temporal lag relative to the IR measurements is to be expected, as is a higher $Q(H_2O)$ measured by *SOHO* if, for example, additional H_2O was released from icy grains in regions of the coma outside those covered by the CSHELL slit.

In our ensuing discussion of the evolution of molecular abundances with $Q(H_2O)$ (Section 4.2.2), we associate the points corresponding to anomalously high water production with "outbursts" that are likely connected with these two events. Similarly, we associate the 25 points used for the heliocentric fit shown in Figure 4 with periods we take to represent the "baseline" (i.e., longer-term) heliocentric evolution in activity.

It is worth comparing our values for $Q(H_2O)$ with those reported for Comet ISON by Dello Russo et al. (2016). They present results from UV, optical, and radio, together with IR observations, using NIRSPEC and CSHELL. Of particular interest is that Dello Russo et al. also see an increase in water production after UT $\sim$ 20 hr on November 19, the date in common with the study reported here, and their mean value for $Q(H_2O)$ on that date ($(2.70 \pm 0.30) \times 10^{29}$ s^{-1}) is consistent with the mean we find based on the six values listed in Table 2 ($(2.58 \pm 0.31) \times 10^{29}$ s^{-1}). We next present abundance ratios for trace species, noting that it is critical to compare not only production rates of trace molecules but also water production rates (see Section 4.2.3).

4.2. Molecular Abundances in Comet ISON

We determined production rates and abundances relative to H_2O (i.e., abundance ratios) for eight molecular species over the range in heliocentric distance $R_h = 1.213$–0.344 AU: CO, C_2H_6, CH_4, CH_3OH, NH_3, H_2CO, HCN, and C_2H_2. We studied the composition of Comet ISON as material was shed and interior regions were exposed to increasingly intense solar irradiation.

Abundance ratios are listed in Table 2, and are shown by molecule in Figure 5, in which (as with the H_2O measurements in Figure 4) error bars represent $\pm1\sigma$ uncertainties; downward-pointing arrows represent 3σ upper limits. The dashed horizontal lines represent weighted mean molecular abundance ratios for ISON based on the encompassed values. For molecules with 3σ upper limits on multiple dates (CO in Figure 5(a), and NH_3 in Figure 5(d)), dotted horizontal lines and accompanying downward-pointing arrows indicate the combined 3σ upper limit.

For all dates, Table 2 lists (in bold) values of $Q(H_2O)$ from which abundance ratios of trace molecules (expressed in percent) were determined. Through November 18, molecular abundances are expressed as the ratio of molecular production rates to the *daily mean* of $Q(H_2O)$, listed as the last line of entries in Table 2 for each date. On November 19, species in C2H6_A (C_2H_6 and CH_3OH), HCN_A (HCN, C_2H_2, and NH_2), and H2O_3C (NH_3) were referenced to $Q(H_2O)$ in interval 1 (these settings span the UT interval 17:00–19:45), and H_2CO was referenced to $Q(H_2O)$ from OH^* in interval 2 (as co-measured in the H2CO_A setting, spanning UT 19:55–20:40). Interval 3 (UT 22:08–23:30) included only two settings (H2O_5A and H2O_3B), from which we report production rates for H_2O only.

On November 22, production rates in settings done immediately prior to (C2H6_A) and following (HCN_A) the

first series of H2O_3A spectra were referenced to the value of $Q(H_2O)$ from interval 1 (spanning UT 17:43–18:01). Comparison with molecular production rates bracketing this measurement of H_2O is appropriate, given the dramatic decrease in water production between the time of these settings and the second series of H2O_3A. This decrease was documented in Paper 1, and is borne out through our investigation of HDO in ISON (Gibb et al. 2016). Production rates of trace species in subsequent settings (beginning with CO in the CO_K setting, and spanning UT 19:25–23:14; see Table 2) were referenced to the mean water production rate observed in interval 2, based on the consistency of $Q(H_2O)$ among its four values—those from the second set of H2O_3A, from CO_K, from the third set of H2O_3A, and from H2O_3C. Accordingly, these comparative water production rates on November 19 and 22, together with simultaneously or contemporaneously measured production rates (and abundance ratios) of trace volatiles, are grouped at appropriate locations in Table 2.

In discussing the evolution in molecular abundance ratios as ISON approached the Sun, we present two different comparisons: (1) their dependence on heliocentric distance and (2) their dependence on total water production. Although related, because of the "outbursts" associated with Events 1 and 2, $Q(H_2O)$ did not show a strictly monotonic increase with decreasing R_h. For this reason, discussing these comparisons separately is instructive.

In Table 2 we also report column densities within the nucleus-centered aperture for all measured species. Known to be a product species, quantifying NH_2 in comets requires modeling the outflow using a Haser and/or vectorial type formalism, and treating it as a parent volatile (on which our formalism for determining production rates is based) is not strictly correct. For this reason, rather than reporting NH_2 production rates on November 7, 19, and 22 ($R_h = 0.83$, 0.46, and 0.35 AU; Table 1), we express abundance ratios for NH_2 by comparing its column density with that of simultaneously (or contemporaneously) measured H_2O (see Table 2, note j).

4.2.1. Evolution of Abundance Ratios with Heliocentric Distance

The first and only apparition of Comet ISON permitted serial measurements of its activity over an unprecedented range of heliocentric distances near and (especially) to well within $R_h = 1$ AU. The abundance ratios of several molecules were largely independent of R_h. In particular, CO, C_2H_6, and CH_4 (Figures 5(a)–(b)) showed relatively little variation with heliocentric distance. Most values were within 1σ (and all were within 2σ) of their respective mean values. The distribution of values for CH_3OH (Figure 5(c)) showed somewhat more scatter, and its mean abundance within $R_h = 0.5$ AU was larger than outside 0.5 AU (Table 3), by a factor of 1.6 ± 0.2. This exceeded stochastic expectations; thus, variability in the abundance ratio of CH_3OH with (presumed) depth in the nucleus cannot be ruled out.

Within heliocentric distance 0.5 AU, NH_3, H_2CO, and HCN showed substantially increased abundance ratios compared to their values at larger R_h (Figures 5(d)–(f)). NH_3 increased by a factor of at least 4.5, the lower limit to its increase being established by the ratio of its mean abundance from November 19 and 22 (3.51%) to the 3σ upper limit obtained by combining values from October 22, 24, and 25 and November 7, spanning $R_h = 1.21$–0.83 AU ($Q(NH_3)/Q(H_2O) < 0.78\%$; see Figure 5(d) and Table 3). H_2CO increased by a factor of 5.6 ± 2.1 on November 19 compared to the mean of its abundances on October 25 and November 7 ($0.16\% \pm 0.05\%$). HCN increased by a factor of 4.4 ± 1.0 compared to its abundance on November 7. The mean of C_2H_2 abundances on November 19 and 22 ($0.24\% \pm 0.02\%$) was higher than that measured on November 7 (Figure 5(g)); however, this increase (by a factor of 2.1 ± 0.8) is less than 3σ and therefore, although suggestive, should be considered less secure than those of NH_3, H_2CO, and HCN.

The ratios of column densities of NH_2 to those of H_2O measured simultaneously (on November 7) or contemporaneously (on November 19 and 22) indicate that NH_2/H_2O increased from 0.28% at $R_h = 0.83$ AU to considerably higher values (approaching or exceeding 1%) inside 0.5 AU. The value on November 7 is somewhat lower than the "typical" value for NH/OH measured among comets (~0.43%) based on the optical survey in A'Hearn et al. (1995). The much broader spatial distribution of NH_2 on November 22 compared to November 19 likely contributed to the different column measurements on these two dates. This is discussed further in Section 5.2.

4.2.2. Relation of Abundance Ratios to Measured Water Production Rates

In Figure 5, we show in red measurements obtained during periods of enhanced water production, on November 15 following "Event 1," and bracketing "Event 2" on November 19 and November 22. We found that overall the abundance ratios of molecules measured in Comet ISON were independent of the total H_2O production rate. Specifically, CO, C_2H_6, CH_4, and CH_3OH were measured during periods of both "baseline" and "outburst" activity, and overall their abundance ratios showed no systematic differences in this regard. For example, the abundance for CH_3OH at 0.46 AU was obtained during "baseline" activity and that at 0.35 AU was obtained during "outburst," yet these agree to well within their 1σ uncertainties (see also Table 2, and Figure 5(c)). Similarly, the abundance ratios measured for HCN (and for C_2H_2) on November 19 and 22 were in agreement even though the first measurements (at 0.46) corresponded to "baseline" water production while the second measurements (at 0.35 AU) were referenced to $Q(H_2O)$ obtained during a period of "outburst" that was presumably associated with Event 2. The situation for NH_3 is inconclusive since it was measured only during "baseline" periods, on both November 19 and November 22. The comparison for H_2CO is also inconclusive since it was measured only once inside 0.5 AU (on November 19), at which time $Q(H_2O)$ was apparently transitioning from "baseline" to "outburst" regimes.

4.2.3. Comparisons with Other Reported Abundance Measurements in Comet ISON

Our combined 3σ upper limit for the CO abundance ratio from October 22 and 24 (2.13%) is consistent with values measured from CSHELL observations on November 15, 16, 17, and 22. It is also consistent with the value reported from *Hubble Space Telescope* observations on October 21 (~1.5%; Weaver et al. 2013) and with the 3σ upper limit reported from preliminary analysis of the NIRSPEC observations on October 22 and 24 (2.0%; Mumma et al. 2013).

The reported preliminary value for CH_3OH from October 22 and 24 ($1.1\% \pm 0.3\%$; Mumma et al. 2013) agrees with our result

from these two dates combined (1.4% ± 0.5%). The preliminary value for C_2H_6 (0.21% ± 0.05%; Mumma et al. 2013) is lower than our corresponding combined value from October 22 and 24 (0.45% ± 0.09%), but is consistent (at the 1σ level) with our value for $R_h > 0.5$ AU (0.28% ± 0.02%; see Table 3). Our abundances for CH_4 and HCN, respectively, are consistent with preliminary values, both from October 22 and 25 (0.7% ± 0.3% and <0.1%, 3σ; Mumma et al. 2013) and from November 7 (0.4% ± 0.1% and 0.06% ± 0.02%; Paganini et al. 2013).

Faggi et al. (2015) obtained an upper limit (3σ) of 2.5×10^{29} s^{-1} for NH_3 production on UT November 26 ($R_h \approx 0.17$ AU) based on the (1, 1) rotational line at 23.7 GHz, using the Medicina 32 m radio antenna. Extrapolating our heliocentric fit for water production ($Q(H_2O) = 1.9 \times 10^{28} R_h^{-3.1}$; Figure 4) to 0.17 AU implies $Q(H_2O) = 4.6 \times 10^{30}$ s^{-1}. This suggests an abundance ratio $Q(NH_3)/Q(H_2O) < 5.5\%$, consistent with our values for NH_3 from November 19 and 22 (Tables 2 and 3).

It is instructive to compare the molecular abundance ratios we find on November 19 with those reported by Dello Russo et al. (2016), as this is the only date for which results are presented both here and in that paper. For the most part these agree within their 1σ uncertainties, the notable exception being that our value for CH_3OH (1.7% ± 0.2%) is substantially larger than that found by Dello Russo et al. (1.2% ± 0.3%). However, the Dello Russo et al. value is based on their overall mean H_2O production rate ($(2.70 \pm 0.30) \times 10^{29}$ s^{-1}), whereas our value uses the mean of the three water measurements spanning interval 1 on November 19 ($(2.25 \pm 0.08) \times 10^{29}$ s^{-1}; see Table 2 and discussion in Section 4.2). Comparing our methanol production rate with our overall mean $Q(H_2O)$ from this date ($(2.58 \pm 0.31) \times 10^{29}$ s^{-1}) results in an abundance ratio for CH_3OH of 1.5% ± 0.3%, consistent with the Dello Russo et al. value at the 1σ level. Furthermore, our abundance ratio for CH_3OH on this date is consistent with those we measured on November 18 (sampling the ν_3 Q-branch at 2844 cm^{-1}) and 22 (sampling the same feature measured on November 19, peaked near 2982 cm^{-1}). Taking the ratios of our November 19 production rates for C_2H_6, HCN, and C_2H_2 (the three other molecules measured within interval 1) to our overall mean $Q(H_2O)$ also revises our abundance ratios (Table 2) for these three species downward somewhat, to 0.29% ± 0.05%, 0.31% ± 0.05%, and 0.21% ± 0.03%, respectively, again consistent with the values reported by Dello Russo et al., and also with the values in Table 2 based on $Q(H_2O)$ from interval 1 on November 19.

This overall agreement between our results and those of Dello Russo et al. lends credibility to both analyses, which were conducted independently, and provides an estimate of the systematic uncertainties associated with treating these data. Systematic errors are generally difficult to assess, and the independent approaches used to analyze the November 19 ISON spectra afford one such opportunity. Factors contributing to systematic uncertainties include molecular fluorescence g-factor, terrestrial atmospheric transmittance correction (especially telluric water burden), choice of continuum baseline level underlying and local to (in frequency) superimposed emissions, and absolute flux calibration (Γ in Table 1).

4.2.4. Taxonomy of Parent Volatile Abundances: Placing ISON in Context

As a working hypothesis, it is conventional to classify comets as "organics normal," "organics depleted," or "organics enriched," based on their abundances of the four organic molecules C_2H_6, CH_3OH, HCN, and C_2H_2 relative to H_2O (e.g., see reviews by Mumma & Charnley 2011; DiSanti & Mumma 2008; Bockelée-Morvan et al. 2004, and references therein). However, these taxonomic classifications depend on existing (i.e., current) mean or median abundances among measured comets and can evolve as the number of comets studied increases. For this reason, it is more meaningful to cite abundance ratios relative to H_2O rather than taxonomic status (depleted, normal, enriched) when comparing results among observers.

Table 3 provides a summary of abundance ratios for Comet ISON and for comparison includes current mean (or for some molecules, median) values that cluster around common values for a fraction of measured comets from the Oort Cloud—for purposes of discussion only, we refer to these as "current normal" values, or "current norms" (see Table 3 note c). The current norms for C_2H_6, CH_3OH, and HCN are consistent with those quoted previously (i.e., in the review papers cited above); however, that for C_2H_2 is lower by a factor of approximately two based on the larger (and continually growing) number of measured comets.

Species having abundance ratios that did not vary significantly with heliocentric distance (CO, C_2H_6, and CH_4; Figures 5(a)–(b)) were depleted in ISON, by factors of two or more compared to their current norms. This was also the case with CH_3OH for $R_h > 0.5$ AU; however, within 0.5 AU its abundance was closer to "normal." For $R_h > 0.5$ AU, H_2CO and HCN were also depleted; however, for $R_h < 0.5$ AU they were enriched by differing amounts (by factors of ~3.6 and 1.8 relative to their respective current norms). The 3σ upper limit measured for NH_3 from 1.21 to 0.83 AU was consistent with its current norm, but for $R_h < 0.5$ AU it was enriched by a factor of 4.7. According to this taxonomic classification, at $R_h = 0.83$ AU C_2H_2 was consistent with its current norm, but was enriched by a factor of ~2 within 0.5 AU. We note, however, that according to the review papers cited above the value for C_2H_2 at 0.83 AU classifies it as "depleted," while for $R_h < 0.5$ AU it is in the "normal" range.

4.3. Comparison with Measurements of Previous Comets at Multiple R_h within 1 AU

Serial measurements of cometary composition exist for a limited number of comets, and even when present for the most part they have been conducted over a restricted range of heliocentric distances exceeding 1 AU. A notable study extending to small R_h is represented by the observations of C/2002 X5 Kudo-Fujikama at $R_h = 1.2$, 0.5, and 0.21 AU, using the IRAM 30 m and Nançay radio telescopes (Biver et al. 2011). Abundance ratios for both HCN and HNC relative to H_2O increased by approximately twofold at 0.21 AU compared to the mean of their respective values at $R_h = 0.5$ and 1.2 AU, while that of CH_3OH remained constant. The results for Comet ISON reported here stand apart from that, as well as from all previous studies, in that they encompass measurements of many species based on observations from beyond $R_h = 1$ AU together with daily measurements that differed substantially in heliocentric distance and extended to within $R_h = 0.35$ AU.

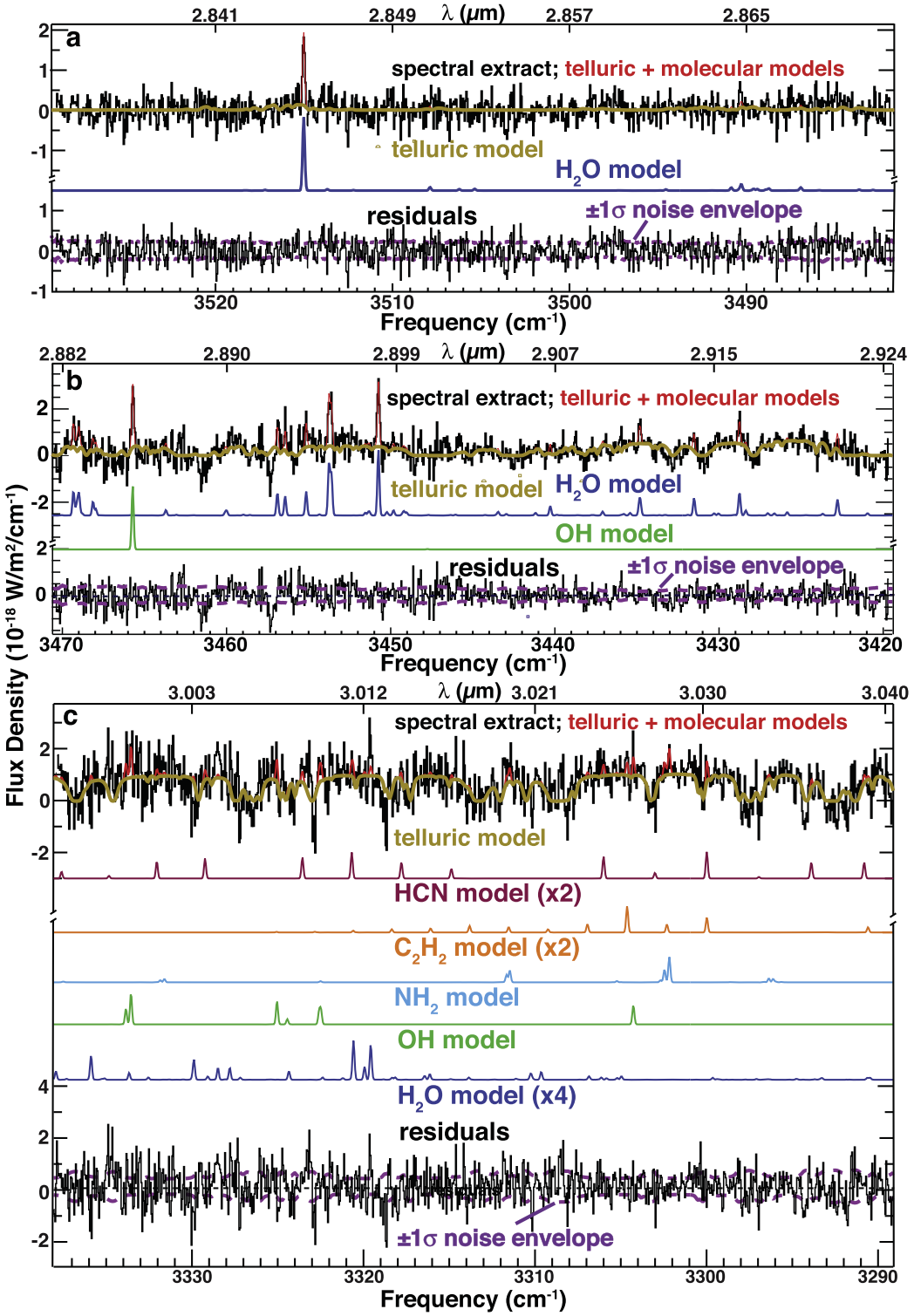

Figure 1. Representative spectral extracts (upper black trace in each panel) from NIRSPEC observations of Comet ISON, showing the integrated signal within a 0.43 × 1.78 arcsec aperture centered on the peak emission intensity. UT dates, NIRSPEC settings, and echelle orders are as follows (here, and in Figure 2; see Table 1 for details including on-source integration times): (a) October 22 KL1, order 27. (b) October 22 KL2, order 26. (c) November 7 KL2, order 25. Here and in Figure 2 the red trace represents the sum of telluric (modeled continuum, gold trace) and cometary components (color-coded by molecule), and the bottom trace (labeled "residuals") represents spectral extract minus the red trace, together with the corresponding $\pm 1\sigma$ stochastic noise envelope (dashed purple traces). For each panel, the lower axis is wavenumbers and the upper axis is equivalent wavelength.

4.4. Comparisons with Interstellar Ices

It is also interesting to compare molecular abundances in Comet ISON with those observed in ices toward protostellar sources. A reanalysis of observations from the *Spitzer* survey of about 50 low-mass and 9 high-mass sources resulted in mean abundance ratios relative to H_2O (Gibb et al. 2004; Öberg et al. 2011); these are included in Table 3. These ice abundances are generally larger than the "normal" abundances found among

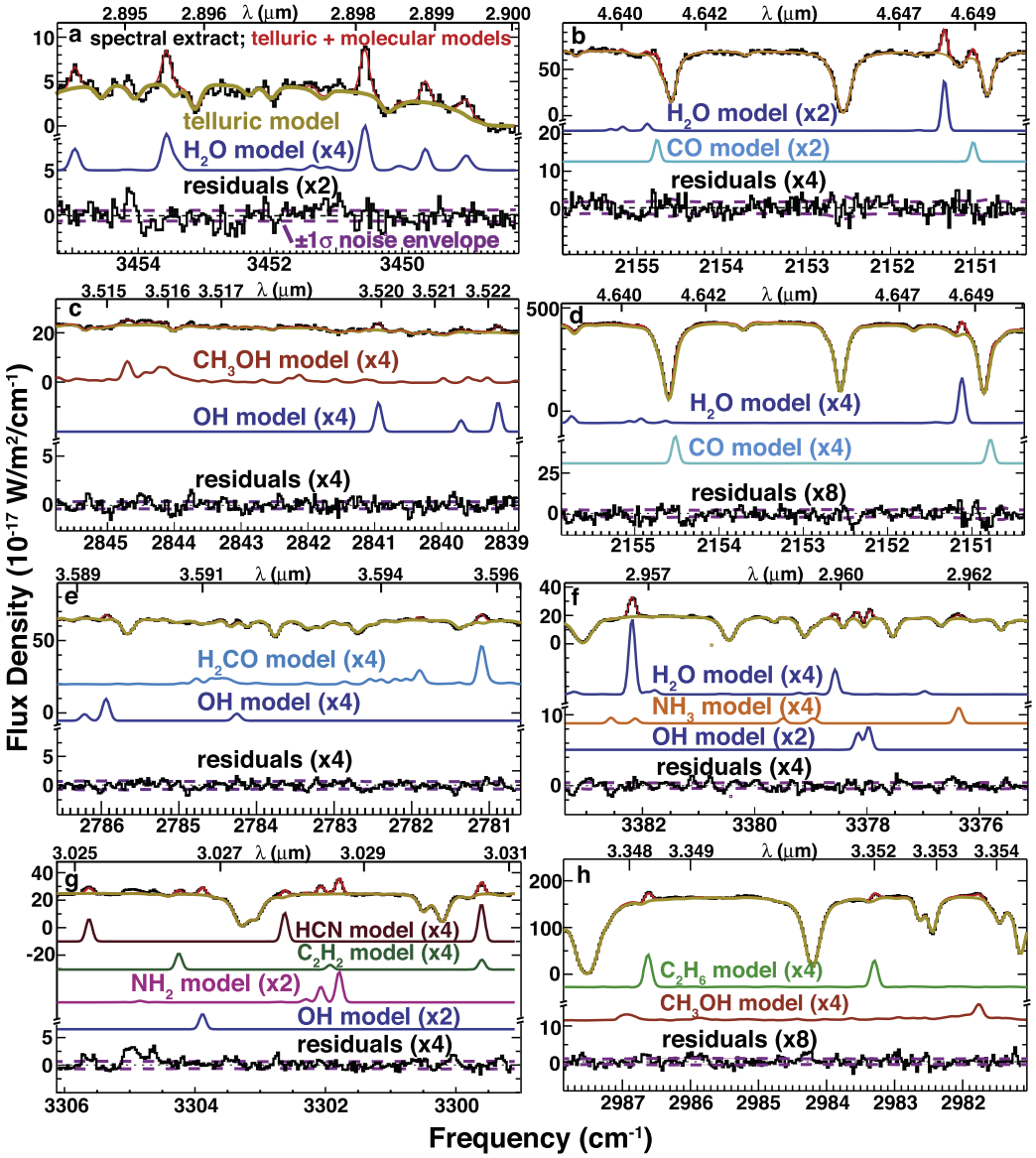

Figure 2. Representative spectral extracts from CSHELL observations of ISON showing the integrated signal within a 1.0 × 3.0 arcsec aperture centered on the peak emission intensity for the following UT dates and settings: (a) November 15, H2O_3A. (b) November 15, CO_K. (c) November 18, CH3OH_A. (d) November 22, CO_K. (e) November 19, H2CO_A. (f) November 19, H2O_3C. (g) November 19, HCN_A. (h) November 22, C2H6_A.

comets; however, for some molecules comparable abundances are observed in certain comets, in particular those classified as "organics enriched." For example, in C/2001 A2 (LINEAR; Magee-Sauer et al. 2008) CH_4 approached the median abundance found toward high-mass sources, HCN was consistent with the median value for X-CN (normally attributed to OCN^-) toward high-mass sources, and CH_3OH was consistent with the median value observed toward low-mass sources. The CO abundance ratio in "CO-rich" comets, as shown in Figure 5 of Paganini et al. (2014), is similar to the median among high-mass sources. The median abundance of NH_3 observed toward both low- and high-mass protostellar sources (5%) is well above the current norm found among comets (0.75%) and higher than that observed to date in any comet, although the value we report for ISON inside $R_h = 0.5$ AU (3.5%) is closest to the interstellar value. Observed differences in molecular abundances in comets (including ISON) versus interstellar ice abundances may indicate additional processing of ices in the protosolar disk or, for comets captured from a neighboring Oort Cloud (as proposed by Levison et al. 2010), in the disks of stars in the Sun's birth cluster.

5. INTERPRETATION OF SPATIAL DISTRIBUTIONS

5.1. Spatial Distributions of Emissions as Diagnostics of Release Mechanisms in Comet ISON

Figure 6 shows additional spatial profiles of emission in Comet ISON. Panels there and in Figure 3 are labeled by CSHELL setting and show co-measured profiles of emitting gaseous species and dust continuum, plus a representative measure of the seeing based on a stellar (focus or standard star) profile measured close in time to the comet observations; this is approximated by the trace labeled "PSF." All profiles are scaled to a common maximum, based on their intensities integrated over the central ±1.5 arcsec. This permits comparison of

Table 2
Molecular Production Rates and Abundances in C/2012 S1 (ISON)

UT Date 2013	T_{rot} K[a]	Setting	Telluric H_2O[b] (pr-mm)	Species	fx_01[c]	Q_{nc}[d] 10^{26} mol s^{-1}	N[e] 10^{14} cm^{-2}	GF[f]	Q_{tot}[g] 10^{26} mol s^{-1}	Q_x/Q_{H2O}[h]
				NIRSPEC						
Oct 22	52 ± 19	KL1, o27	(5.19)	H_2O	0.00914	59.8 ± 9.0	6.77 ± 1.01	1.72 ± 0.12	103 ± 17	
	(52)	o26		H_2O		71.2 ± 11.1	8.06 ± 1.26	(1.72 ± 0.12)	122 ± 21	
	(52)	o26		NH_3	0.146	<1.96	<0.189	(1.72 ± 0.12)	<3.36	<**3.05**
	(52)	o23		C_2H_6	0.00776	0.329 ± 0.088	0.0373 ± 0.0102	(1.72 ± 0.12)	0.564 ± 0.157	**0.512 ± 0.154**
	(52)	o22(,o23)		CH_3OH	0.00850	1.04 ± 0.47	0.117 ± 0.053	(1.72 ± 0.12)	1.78 ± 0.81	**1.61 ± 0.75**
	(52)	MW, o16	(4.60)	CO	0.00186	<1.65	<0.187	(1.72 ± 0.12)	<2.84	<**2.57**
				H_2O		**64.3 ± 7.0**	7.278 ± 0.790		110 ± 14	
Oct 24	(50)	KL1, o27	(4.14)	H_2O	0.00925	56.0 ± 4.8	6.467 ± 0.560	1.61 ± 0.10	90.4 ± 9.6	
	(50)	o26		H_2O		61.3 ± 10.2	7.074 ± 1.176	(1.61 ± 0.10)	98.9 ± 17.5	
	(50)	o26		NH_3	0.148	<1.67	<0.164	(1.61 ± 0.10)	<2.70	<**2.93**
	(50)	o23		C_2H_6	0.00785	0.236 ± 0.059	0.0273 ± 0.0070	(1.61 ± 0.10)	0.381 ± 0.098	**0.414 ± 0.107**
	(50)	o22(,o23)		CH_3OH	0.00859	0.695 ± 0.358	0.0804 ± 0.0416	(1.61 ± 0.10)	1.12 ± 0.58	**1.22 ± 0.64**
	(50)	MW, o16	(5.60)	CO	0.00186	<2.16	<0.249	(1.61 ± 0.10)	<3.49	<**3.78**
				H_2O		**57.0 ± 4.4**	6.579 ± 0.505		92.4 ± 8.4	
Oct 25	(50)	KL2, o26	(2.40)	H_2O	0.00933	44.4 ± 8.4	5.181 ± 0.978	1.42 ± 0.22	63.0 ± 15.4	
	(50)	o25		HCN	0.0104	<0.0510	<0.00624	(1.42 ± 0.22)	<0.0723	<**0.117**
	(50)	o25		C_2H_2	0.00969	<0.106	<0.0140	(1.42 ± 0.22)	<0.150	<**0.242**
	(50)	o25		NH_3	0.149	<0.800	<0.0793	(1.42 ± 0.22)	<1.14	<**1.83**
	(50)	o23		OH^*	0.0093	40.3 ± 18.0	4.703 ± 2.114	(1.42 ± 0.22)	57.2 ± 27.0	
	(50)	o23		CH_4	0.0056	0.100 ± 0.032	0.0115 ± 0.0028	(1.42 ± 0.22)	0.142 ± 0.051	**0.224 ± 0.065**
	(50)	o21		H_2CO	0.126	0.121 ± 0.043	0.0094 ± 0.0034	(1.42 ± 0.22)	0.171 ± 0.066	**0.276 ± 0.108**
				H_2O		**43.7 ± 7.6**	5.097 ± 0.888		62.0 ± 14.2	
Nov 7	(70)	KL2, o26	(2.42)	H_2O	0.0113	202 ± 18	26.82 ± 2.36	1.98 ± 0.30	400 ± 71	
	(70)	o25		HCN	0.0126	0.156 ± 0.032	0.0206 ± 0.0044	(1.98 ± 0.30)	0.308 ± 0.080	**0.074 ± 0.016**
	(70)	o25		C_2H_2	0.0109	0.236 ± 0.085	0.0312 ± 0.0114	(1.98 ± 0.30)	0.466 ± 0.183	**0.111 ± 0.040**
	(70)	o25		NH_3	0.176	<1.99	<0.219	(1.98 ± 0.30)	<3.82	<**0.939**
	(70)	o25		NH_2	0.0140		0.078 ± 0.015			***0.276 ± 0.057***[j]
	(70)	o25		OH^*	0.0113	201 ± 54	26.63 ± 7.32	(1.98 ± 0.30)	397 ± 123	
	(70)	o24		OH^*	0.0113	259 ± 50	34.31 ± 6.88	(1.98 ± 0.30)	512 ± 126	
	(70)	o23		OH^*	0.0113	237 ± 47	31.45 ± 6.25	(1.98 ± 0.30)	469 ± 118	
	(70)	o23		CH_4	0.00874	0.804 ± 0.091	0.107 ± 0.013	(1.98 ± 0.30)	1.59 ± 0.30	**0.380 ± 0.045**
	(70)	o22		C_2H_6	0.00963	0.561 ± 0.153	0.0748 ± 0.0208	(1.98 ± 0.30)	1.11 ± 0.35	**0.265 ± 0.073**
	(70)	o21		OH^*	0.0113	290 ± 75	38.37 ± 10.09	(1.98 ± 0.30)	572 ± 172	
	(70)	o21		H_2CO	0.148	0.298 ± 0.100	0.0336 ± 0.0113	(1.98 ± 0.30)	0.588 ± 0.216	**0.141 ± 0.047**
				H_2O		**212 ± 13**	***28.34 ± 1.98***		440 ± 48	

UT Date 2013	T_{rot} K[a]	Setting	Telluric H_2O[b] (pr-mm)	Species	fx_01[c]	Q_{nc}[d] 10^{26} mol s^{-1}	N[e] 10^{14} cm^{-2}	GF[f]	Q_{tot}[g] 10^{26} mol s^{-1}	Q_x/Q_{H2O}[h]
				CSHELL						
Nov 15	**104 ± 2**	H2O_3A	(6.29)	H_2O	0.0303	1600 ± 48	105 ± 6	1.59 ± 0.08	2537 ± 198	
	(104)	CO_K	8.11	CO	0.00186	22.0 ± 1.7	1.49 ± 0.14	1.64 ± 0.07[‡]	36.1 ± 3.2	**1.51 ± 0.17**
	(104)			H_2O	0.0304	1330 ± 57	86.8 ± 5.8	1.64 ± 0.07[‡]	2176 ± 171	
	(104)	CH4_E	6.91	CH_4	0.0184	4.50 ± 0.71	0.30 ± 0.05	1.73 ± 0.20[‡]	7.76 ± 1.31	**0.325 ± 0.059**
	(104)			OH^*	0.0305	1560 ± 117	102 ± 9	1.73 ± 0.20[‡]	2686 ± 287	

Table 2
(Continued)

UT Date 2013	T_{rot} K[a]	Setting	Telluric H_2O[b] (pr-mm)	Species	fx_01[c]	Q_{nc}[d] 10^{26} mol s^{-1}	N[e] 10^{14} cm^{-2}	GF[f]	Q_{tot}[g] 10^{26} mol s^{-1}	Q_x/Q_{H2O}[h]
				CSHELL						
	(104)	C2H6_A	7.10	C_2H_6	0.0261	5.18 ± 0.20	0.34 ± 0.02	1.60 ± 0.08	8.27 ± 0.51	**0.346 ± 0.032**
	(104)			CH_3OH	0.0285	17.1 ± 2.0	1.12 ± 0.14	(1.60 ± 0.08)	27.3 ± 3.5	**1.14 ± 0.17**
				H_2O					**2390 ± 118**	
Nov 16	**89 ± 5**	H2O_3A	(3.03)	H_2O	0.0322	628 ± 42	40.5 ± 3.4	1.44 ± 0.08	905 ± 79	
	(89)	CO_K	2.89	CO	0.00200	3.34 ± 0.89	0.22 ± 0.06	2.39 ± 0.22‡	8.26 ± 2.29	**0.907 ± 0.265**
	(89)			H_2O	0.0327	386 ± 27	24.7 ± 2.1	2.39 ± 0.22‡	921 ± 107	
				H_2O					**911 ± 72**	
Nov 17	**107 ± 3**	H2O_3A	2.55	H_2O	0.0347	1360 ± 79	85.3 ± 5.0	1.36 ± 0.04	1827 ± 130	
	(107)	CO_K	2.61	CO	0.00217	12.2 ± 1.6	0.79 ± 0.10	1.84 ± 0.17‡	22.4 ± 3.4	**1.34 ± 0.11**
	(107)			H_2O	0.0352	756 ± 56	47.8 ± 3.6	1.84 ± 0.17‡	1394 ± 167	
	$105^{+7}/_{-6}$	H2O_3A	2.81	H_2O	0.0353	626 ± 55	39.2 ± 3.4	2.69 ± 0.16	1680 ± 177	
	(105)	C2H6_A	2.73	C_2H_6	0.0302	2.21 ± 0.17	0.14 ± 0.01	1.89 ± 0.20‡	4.19 ± 0.49	**0.251 ± 0.020**
	(105)			CH_3OH	0.0329	8.54 ± 1.38	0.54 ± 0.09	1.89 ± 0.20‡	16.2 ± 3.0	**0.969 ± 0.076**
				H_2O					**1668 ± 131**	
Nov 18	(100)	CH3OH_A	(1.85)	CH_3OH	0.0350	14.0 ± 1.0	0.86 ± 0.06	1.77 ± 0.09	24.8 ± 2.1	**1.54 ± 0.16**
	(100)			OH*	0.0376	1150 ± 77	71.1 ± 4.7	1.52 ± 0.10	1740 ± 162	
	100 ± 4	H2O_3A	2.01	H_2O	0.0376	652 ± 46	40.0 ± 2.8	2.35 ± 0.11	1532 ± 131	
				H_2O					**1615 ± 102**	
Nov 19	(112)	H2O_3B	2.33	H_2O	0.0413	1390 ± 76	82.6 ± 4.5	1.60 ± 0.06	2233 ± 147	
	(112)	C2H6_A	2.34	C_2H_6	0.0353	4.81 ± 0.42	0.29 ± 0.03	1.58 ± 0.07‡	7.59 ± 0.75	**0.337 ± 0.035**
	(112)			CH_3OH	0.0385	24.7 ± 2.1	1.47 ± 0.13	1.58 ± 0.07‡	39.0 ± 3.8	**1.73 ± 0.18**
	112 ± 2	H2O_3A	2.40	H_2O	0.0415	1660 ± 88	98.1 ± 5.2	1.44 ± 0.04	2375 ± 141	
	(112)	HCN_A	2.55	HCN	0.0462	4.24 ± 0.39	0.25 ± 0.02	1.89 ± 0.07	8.01 ± 0.80	**0.356 ± 0.037**
	(112)			C_2H_2	0.0401	2.93 ± 0.24	0.17 ± 0.01	(1.89 ± 0.07)	5.53 ± 0.49	**0.246 ± 0.024**
	(112)			NH_2	0.0511		1.09 ± 0.06			***1.22 ± 0.08***[j]
	(112)	H2O_3C	2.52	H_2O	0.0417	1440 ± 76	87.7 ± 4.5	1.51 ± 0.02	2175 ± 116	
	(112)			NH_3	0.4826	43.7 ± 3.1	1.74 ± 0.12	1.84 ± 0.09	80.4 ± 6.8	**3.58 ± 0.33**
				H_2O			***88.6 ± 2.7***		**2249 ± 77**	
	(112)	H2CO_A	(1.81)	**OH***	0.0419	1770 ± 292	111 ± 18	1.75 ± 0.12	**3098 ± 553**	
	(112)			H_2CO	0.4576	13.5 ± 1.2	0.53 ± 0.05	2.10 ± 0.19	28.2 ± 3.5	**0.911 ± 0.198**
	(112)	H2O_5A	2.80	H_2O	0.0416	1880 ± 100	110 ± 6	2.15 ± 0.06	4042 ± 247	
	(112)	H2O_3B	(2.72)	H_2O	0.0415	1860 ± 98	113 ± 6	2.46 ± 0.04	4573 ± 251	
				H_2O					**4303 ± 310**	
Nov 22	(138)	C2H6_A[i]	1.86	C_2H_6	0.0524	11.5 ± 1.3	0.54 ± 0.03	1.96 ± 0.15	22.5 ± 3.1	**0.227 ± 0.024**
	(138)			CH_3OH	0.0573	63.6 ± 7.9	2.48 ± 0.18	2.62 ± 0.39	167 ± 32	**1.68 ± 0.29**
	138 ± 5	H2O_3A[i]	2.06	**H_2O**	0.0401	6530 ± 296	***486 ± 33***	1.52 ± 0.02	**9920 ± 450**	

Table 2
(Continued)

UT Date 2013	T_{rot} K[a]	Setting	Telluric H_2O[b] (pr-mm)	Species	fx_01[c]	Q_{nc}[d] 10^{26} mol s^{-1}	N[e] 10^{14} cm^{-2}	GF[f]	Q_{tot}[g] 10^{26} mol s^{-1}	Q_x/Q_{H2O}[h]
				CSHELL						
	(138)	HCN_A[i]	1.91	HCN	0.0685	17.3 ± 2.0	0.86 ± 0.05	1.74 ± 0.08	30.2 ± 3.7	**0.304 ± 0.026**
	(138)			C_2H_2	0.0597	13.0 ± 1.7	1.08 ± 0.09	(1.74 ± 0.08)	22.6 ± 3.1	**0.228 ± 0.024**
	(138)			NH_2	0.0754		3.71 ± 0.22			***0.763 ± 0.072***[j]
	134 ± 2	H2O_3A	1.80	H_2O	0.0625	1990 ± 186	102 ± 10	1.94 ± 0.13	3860 ± 440	
	(130)	CO_K	2.31	H_2O	0.0639	1680 ± 99	84 ± 5	2.76 ± 0.15	4617 ± 368	
	(130)			CO	0.00404	41.4 ± 7.7	2.21 ± 0.41	1.82 ± 0.13	75.2 ± 14.9	**1.81 ± 0.37**
	$\mathbf{125^{+9}/_{-7}}$	H2O_3A	2.19	H_2O	0.0639	2280 ± 141	116 ± 7	1.76 ± 0.13	4010 ± 380	
	(125)	H2O_3C	2.05	H_2O	0.0642	1590 ± 154	80.2 ± 7.8	2.52 ± 0.05	4014 ± 397	
	(125)			NH_3	0.6264	56.7 ± 3.7	1.18 ± 0.11	3.36 ± 0.64	152 ± 32	**3.22 ± 0.70**
				H_2O					**4154 ± 197**	

Notes.

[a] Rotational temperature, based on relative intensities among H_2O lines in "nucleus-centered" extract, as defined in note c. Parentheses denote adopted values. All uncertainties in this table represent 1σ, and upper limits represent 3σ.

[b] Atmospheric burden of precipitable water vapor (pwv, in mm of H_2O) used to model the telluric transmittance function, obtained by fitting cometary spectra as discussed in Section 3.1 and Appendix A.1, or (in parentheses) as estimated from CSO tau plots (Section A.2). For NIRSPEC dates, the very weak continuum prevented determining pwv from the comet spectra; thus, values were adopted from accompanying flux standard star spectra, using the CSO tau plots as a guide in estimating values appropriate to the ISON observations.

[c] Fraction $f(x)$ of molecules in the coma included in the nucleus-centered aperture, which was 3 (spectral) × 9 (spatial) pixels (0.43 × 1.78 arcsec) for NIRSPEC, and 5 × 15 pixels (1 × 3 arcsec) for CSHELL (see Section 3.2). The factor *fx*_01 depends on geometric parameters (R_h, Δ) and is based on the following photodissociation lifetimes, τ_1(s): H_2O, 7.7×10^4; CO, 1.3×10^6; C_2H_6, 9.1×10^4; CH_3OH, 8.3×10^4; HCN, 6.9×10^4; C_2H_2, 8.0×10^4; CH_4, 1.3×10^5; H_2CO, 5.0×10^3; NH_3, 4.1×10^3; NH_2, 6.2×10^4.

[d] Nucleus-centered production rate (see Section 3.2.2), which includes ±5% uncertainty in Γ (see Table 1, note d), here and in the corresponding column density (note e).

[e] Column density of emitting species in the nucleus-centered aperture. This is related to nucleus-centered production rate (Q_{nc}) and other parameters as $N = (Q_{nc})(\tau_1)(fx_01)[R_h(\mathrm{AU})]^2/A_{nc}$, where $A_{nc}(\mathrm{cm}^2)$ is the area of the nucleus-centered aperture subtended at the comet ($A_{nc} \approx 4.05 \times 10^{15}$ $[\Delta(\mathrm{AU})]^2$ for NIRSPEC, and 1.58×10^{16} $[\Delta(\mathrm{AU})]^2$ for CSHELL). In this expression for *N*, the numerator is the equivalent column abundance, or the number of molecules (or radicals) contained in the nucleus-centered aperture.

[f] Slit loss factor, used to convert Q_{nc} to total (i.e., global) production rate (Q_{tot}; see note g). Entries in parentheses are assumed and are based on GF measured for one or more simultaneously observed emissions having sufficiently high signal-to-noise ratio. Entries with the superscript ‡ the mean GF is used, based on species co-measured in the same setting and having GFs within 1σ of each other.

[g] Total production rate. All uncertainties in Q_{tot} incorporate those in GF. Values for H_2O shown in bold are comparatives for establishing abundance ratios of trace molecules, as discussed in Section 4.2.

[h] Molecular abundance relative to $H_2O = 100$. For NIRSPEC dates (October 22, 24, 25, and November 7) the GF measured for H_2O was assumed to apply to all measured species, so molecular abundances are represented by ratios of Q_{nc} to that of water. Abundances for all molecules, and comparative $Q(H_2O)$ for each date (through November 18) or UT interval (for November 19 and 22), are shown in bold.

[i] These three settings (C2H6_A, H2O_3A, and HCN_A) on November 22 were affected similarly by vignetting of the beam; this plus ±10% uncertainty are included in tabulated column densities, and also in nucleus-centered and total production rates for C_2H_6, CH_3OH, H_2O, HCN, and C_2H_2 from these settings, to account for uncertainty in the degree of vignetting. Abundance ratios for C_2H_6, CH_3OH, HCN, and C_2H_2were based on $Q(H_2O)$ from the first H2O_3A measurement, but do not include ±10% uncertainty because *differences* in vignetting among these settings are assumed to be negligible since they were done over a short time period.

[j] Values for NH_2 on November 7, 19, and 22 are based on column densities relative to those of H_2O in the equivalent nucleus-centered aperture, with both column abundances for H_2O and abundances for NH_2 shown in ***bold italics***. Establishing robust production rates requires modeling NH_2 as a product species (see Section 5.2).

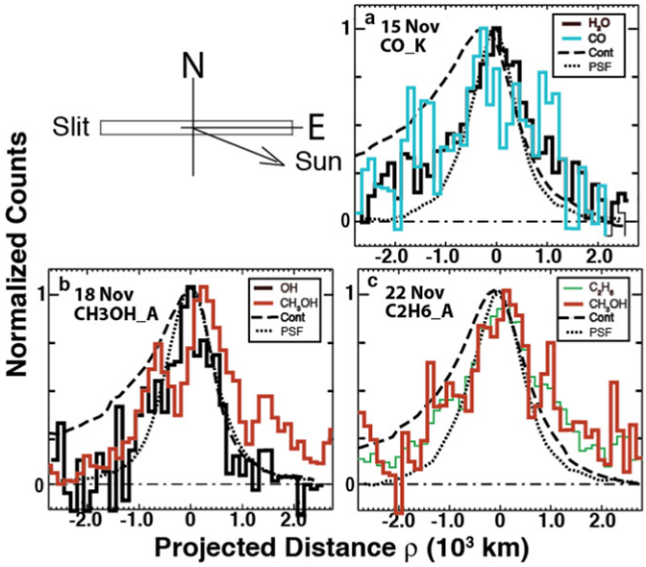

Figure 3. Spatial profiles of emission from simultaneously measured gas and dust continuum in several CSHELL settings. These are used to obtain total production rates and also to assess the nature of volatile release (see Section 3.2.2 and Appendix A.3). The schematic compass in each panel shows the east–west slit orientation and the sunward direction projected on the sky plane. The solar phase angle of ISON remained near 90° from November 15 and 22 (see Section 5.1); thus, the true sunward direction was nearly in the sky plane.

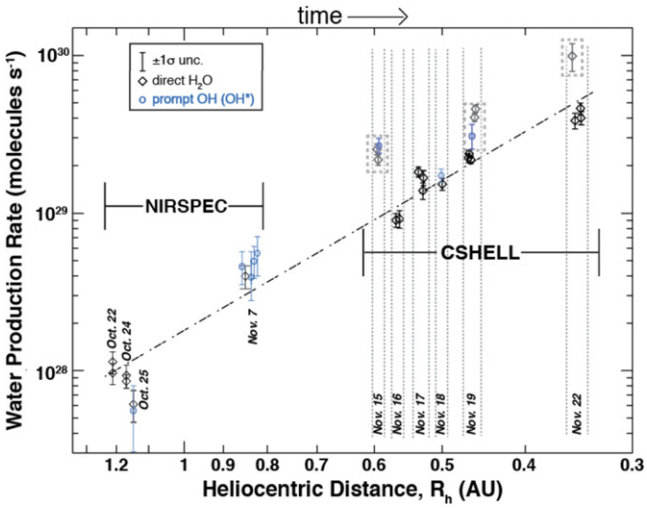

Figure 4. Evolution of water production in Comet ISON spanning 2013 October 22 (R_h = 1.213 AU) through November 22 (R_h = 0.344 AU). The NIRSPEC results were obtained simultaneously on each date; the points on November 7 are separated horizontally only to visualize them more clearly. Of the 32 measurements, 7 (in dashed boxes) were associated with periods of enhanced water production (i.e., with "outbursts"). A heliocentric fit to the remaining 25 points (dot-dashed line) results in a power law ($Q(H_2O) = (1.89 \pm 0.11) \times 10^{28}\, R_h^{(-3.10\pm0.09)}$ molecules s^{-1}).

outflow among volatiles and the dust continuum and allows identification of outflow asymmetries in the coma. These figures show that the dust continuum profile was consistently *asymmetric* (i.e., enhanced) in the antisunward-facing hemisphere (to the left in each panel), and its peak was generally displaced by 1–2 pixels in that direction relative to the co-measured gas.

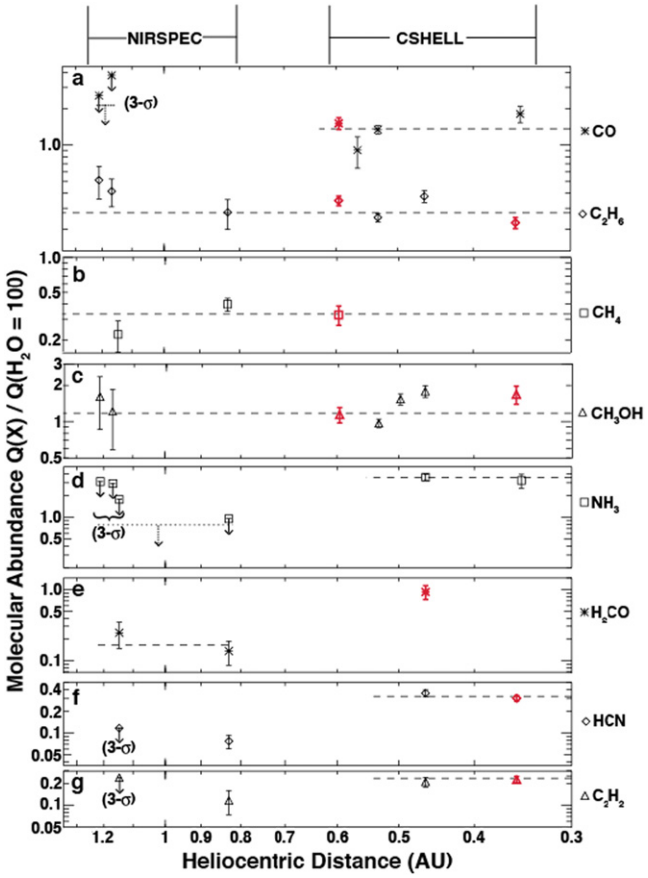

Figure 5. Evolution of molecular abundance ratios relative to H_2O in Comet ISON. Points shown in red were measured during periods of enhanced gas production (i.e., during "outburst"). No discernible dependence of composition on "baseline" vs. "outburst" activity is seen (see Section 4.2.2).

Despite a much stronger thermal signature at smaller R_h, the continuum consistently showed a single peak in the CSHELL observations. We see no evidence for splitting of the nucleus into two or more similar-sized fragment nuclei over the course of the observations, based on the consistent single-peaked continuum profiles (also see Section 6.1 of Paper 1). Typical separation velocities of $\sim$2 m s^{-1} are reported for binary fragments of split comets within R_h = 1 AU (Boehnhardt 2004). If ISON underwent such splitting, dual peaks would become evident within 2–3 days, unless oriented along our line of sight. Even for this case, for example, global splitting of the nucleus associated with "Event 1," it seems unlikely that this orientation would be retained over the period encompassed by the CSHELL observations (approximately 1 week). Such global splitting appears unlikely particularly given the consistently large solar phase angle throughout the period November 15–22, which varied from 80° to 101°; therefore, both the Sun–comet direction and the orbital vector of Comet ISON remained close to the plane of the slit (i.e., to the sky plane). However, given the subsequent complete disruption of ISON near perihelion, the onset of global splitting toward the end of our observing period cannot be ruled out, nor can the ejection from the nucleus of icy chunks of various sizes (see Combi et al. 2014) that were too small to be detected by our observations.

Table 3
Abundances in ISON Compared to Other Comets and Interstellar Sources

Source[a]	CO	C_2H_6	CH_4	CH_3OH	NH_3	H_2CO	HCN	C_2H_2
ISON[b]								
$R_h > 0.5$ AU [b]	*1.3 ± 0.1*	*0.28 ± 0.02*	*0.33 ± 0.03*	*1.1 ± 0.1*	<0.78	*0.16 ± 0.05*	*0.07 ± 0.02*	0.11 ± 0.04
$R_h < 0.5$ AU [b]	*1.8 ± 0.4*	*0.26 ± 0.02*		1.7 ± 0.2	**3.5 ± 0.3**	**0.91 ± 0.20**	**0.32 ± 0.02**	**0.24 ± 0.02**
"Normal" [c]	{4.0}	0.62 ± 0.02	{0.87}	2.2 ± 0.2	0.75 ± 0.23	{0.25}	0.18 ± 0.03	0.11 ± 0.02
73P/S-W3-C [d]	*0.50 ± 0.13*[e]	*0.15 ± 0.04*[f,g]	*<0.25* [g]	*0.14 ± 0.02*[g]	*<0.3*[g]	*0.11 ± 0.02*[g]	0.25 ± 0.02[g]	<0.033[g]
C/1999 S4 [d]	*0.9 ± 0.3*[h]	*0.11 ± 0.02*[h]	*0.12 ± 0.02*[h]	*<0.26*[h]			0.10 ± 0.03[h]	<0.14[h]
C/2001 A2 [i]	3.9 ± 1.1	**1.70 ± 0.20**	**1.2 ± 0.2**	**3.0 ± 0.1**	**1.38 ± 0.37**	0.24-*0.05*	**0.6 ± 0.1**	**0.5 ± 0.1**
Low-mass [j]	29		5	3	5		0.3	
High-mass [j]	13		2	4	5		0.6	

Notes.
[a] Refers to specific comet, type of study, or astronomical source observed.
[b] This work. Mean molecular abundance ratios relative to H_2O (in percent) in Comet ISON are listed separately for $R_h > 0.5$ and $R_h < 0.5$ AU, excluding upper limits except for cases in which only these were obtained (i.e., NH_3 for $R_h > 0.5$ AU). Values in red, black, and blue indicate "organics depleted," "organics normal," and "organics enriched," respectively, as defined by the current compositional taxonomy (see Section 4.2.4).
[c] "Normal" refers to a sample of 12 comets in which C_2H_6 was measured, all of which come from the Oort Cloud, excepting the compositional measurement of the ejecta from Jupiter-family Comet 9P/Tempel 1 (Mumma et al. 2005) resulting from the Deep Impact experiment. Values for CH_3OH, HCN, and C_2H_2 draw on a subset of these: CH_3OH and HCN, 11 comets; C_2H_2, 9 comets. For CO, CH_4, and H_2CO median values are listed since these molecules show larger variations among comets measured to date (from both Oort Cloud and Jupiter-family populations), by factors of 10 or more. The mean value listed for NH_3 is based on 12 comets, 6 of which are in the C_2H_6 group and all excepting 6P/d'Arrest (Dello Russo et al. 2009) are from the Oort Cloud. For all molecules, upper limits are excluded when calculating "normal" (current mean or median) values.
[d] Comets 73P/Schwassmann–Wachmann 3 and C/1999 S4 (LINEAR) are classified as "organics depleted."
[e] DiSanti et al. (2007).
[f] Villanueva et al. (2006).
[g] Dello Russo et al. (2007).
[h] Mumma et al. (2001).
[i] C/2001 A2 (LINEAR) is classified as "organics enriched." Values are adopted from Magee-Sauer et al. (2008) and Gibb et al (2007). H_2CO changed from 0.24% to 0.05% on successive dates at 1.2 AU, and an abundance for CH_4 as high as 3.5% was reported at $R_h = 1.6$ AU (Gibb et al. 2007), suggesting chemical heterogeneity in the nucleus. The value listed for CH_3OH is as revised by Villanueva et al. (2012a)
[j] "Low-mass" and "high-mass" refer to protostellar sources observed by the *Spitzer* survey. Median ice abundances (relative to $H_2O = 100$) are taken from table 2. Öberg et al. (2011); also see Gibb et al. (2004) and see the discussion in Section 4.4.

In Comet ISON the abundance ratios of H_2CO, HCN, and NH_3 were higher by varying amounts within 0.5 AU. However, establishing their abundances as ices in the nucleus requires investigating the extent to which they were released directly from the nucleus as primary volatiles versus their delayed release, for example, from one or more potential progenitor species in the coma. A rigorous study requires detailed modeling of the outflow, allowing for release in the coma using a full vector formalism, and if necessary incorporating optical depth effects. This is outside the scope of the present study.

Nonetheless, it is worthwhile to compare the spatial profiles shown for these molecules in Figure 6. A similar spatial offset was observed between the HCN and dust profiles in ISON obtained with ALMA on 2013 November 15 (Cordiner et al. 2014). However, as discussed in Paper 1—which also shows similar offset and asymmetry in the H2O_3A setting on November 17 and 22—the larger (millimeter-sized) grains sampled by ALMA were slower moving and also less affected by solar radiation pressure, and so they were less extended in the antisunward-facing hemisphere compared to the micron-sized grains to which the CSHELL observations reported here (and in Paper 1) are most sensitive.

5.2. Search for Distributed Volatile Emission

Assuming uniform outflow in the coma at constant speed, in the absence of photodecay the three-dimensional gas density varies as r^{-2}, where r represents distance from the nucleus. Under this assumption, along the line of sight the column density (molecules cm^{-2}) or equivalently the column abundance (molecules in the beam, for example, as shown for H_2O in Figure 3 of Paper 1) varies as ρ^{-1}, where ρ is distance from the cometary nucleus *projected onto the sky plane*. Including photodecay causes a falloff steeper than ρ^{-1}, to a degree dependent on the photodissociation scale length Λ as defined in Section 3.2.2.

5.2.1. Epsilon Profiles

This can be visualized by removing the canonical r^{-2} spatial dependence. We averaged signal from diametrically opposite distances along the profile and multiplied each spatial point along this mean profile by its corresponding projected distance ρ from the nucleus. We refer to the resulting graphical representation as an "epsilon profile" or "epsilon plot," following terminology dating to the study of CN in the coma of Comet 1P/Halley (Komitov et al. 1989).

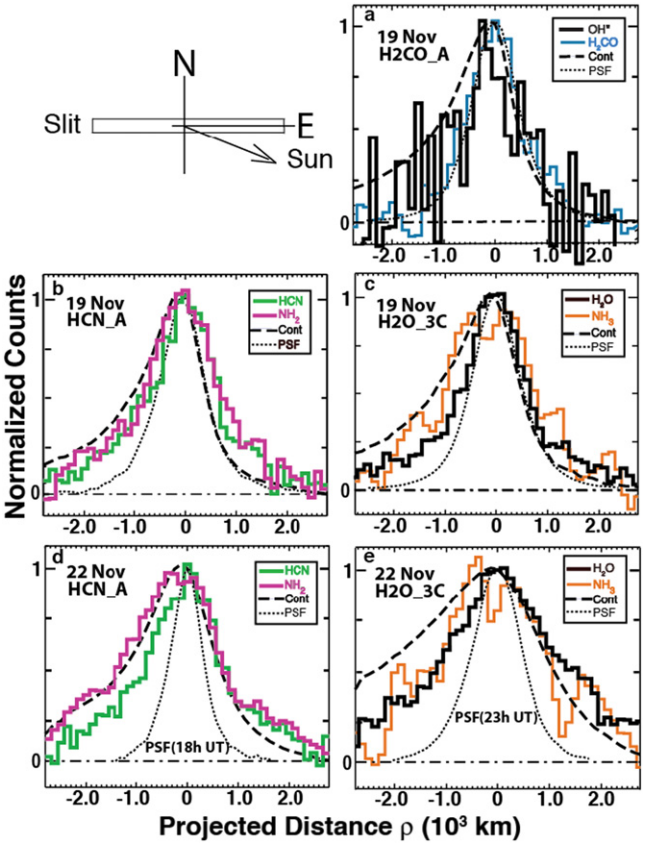

Figure 6. Similar to Figure 3, but for settings containing species that showed pronounced increases in abundance ratio relative to H_2O at $R_h < 0.5$ AU.

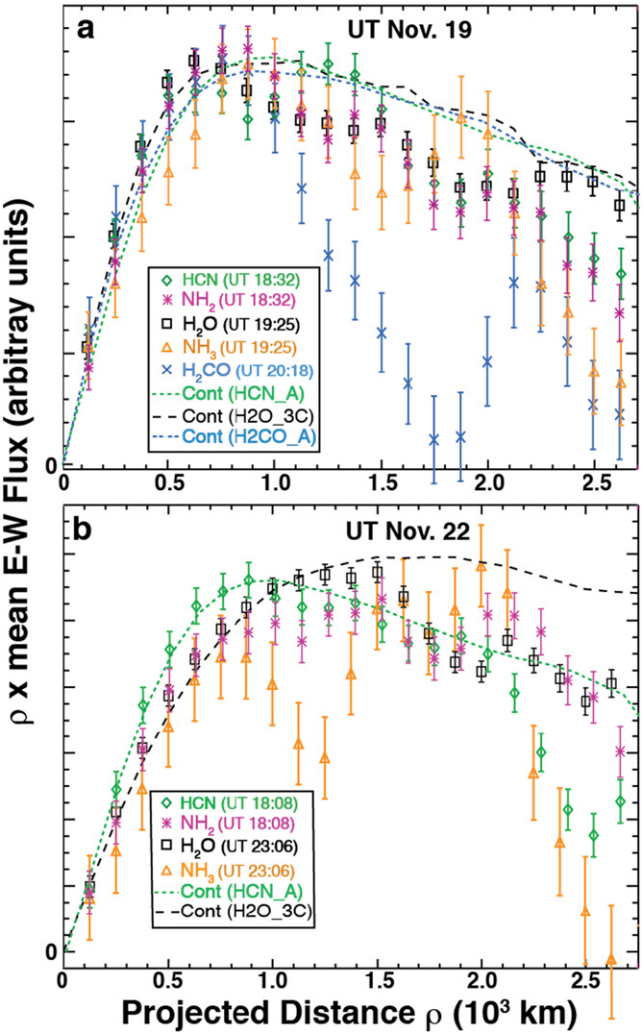

Figure 7. "Epsilon plots" for species with spatial profiles shown in Figure 6. See the discussion in Section 5.2.

Epsilon plots so generated from the profiles in Figure 6 are shown in Figure 7 for emissions from all gaseous species and co-measured continua in three settings on November 19 (HCN_A, H2O_3C, H2CO_A; Figure 7(a)) and two settings on November 22 (HCN_A and H2O_3C; Figure 7(b)). These are color-coded by CSHELL setting (for the continuum) and by molecule, and all are scaled arbitrarily to a common maximum value. This makes it easier to compare shapes and trends with distance from the nucleus, taken to be the zero position on the x-axis.

5.2.2. Dust Continuum

On November 19 (Figure 7(a)), the continuum epsilon profiles from the three included settings tracked each other closely, suggesting that the grain outflow behavior (and seeing) did not vary appreciably over the approximately 2 hr period encompassed by the observations. Their slow decline following a maximum near $\rho = 10^3$ km shows that at larger offset distances the E-W average profile was somewhat steeper than ρ^{-1}.

On November 22 (Figure 7(b)) the observed difference between continuum curves at offsets less than 10^3 km is expected given the poorer seeing conditions during the H2O_3C observations; compare the PSF traces from UT ~ 18 hr and 23 hr UT in Figures 6(d) and (e), respectively. However, the continuum epsilon profiles decline differently for offsets beyond ~1000 km. The shape of the HCN_A continuum on November 22 agrees closely with that seen on November 19 (with column density decreasing faster than ρ^{-1}), while the continuum in the H2O_3C setting indicates an approximately ρ^{-1} falloff. The origin of that difference is likely connected with changing outflow during the 5 hr temporal gap between the two measurements.

5.2.3. Gas

Most emission profiles we measured in Comet ISON, including those of H_2O, were consistent with release directly from the nucleus, or at least were strongly dominated by direct release. However, some subtleties were evident. The relatively steep drop experienced by H_2CO with distance from the nucleus on November 19 (Figure 7(a)) was consistent with its short photodissociation lifetime ($\tau_1 \sim 5 \times 10^3$ s, compared with approximately 8×10^4 s and 7×10^4 s for H_2O and HCN, respectively; Huebner et al. 1992, pp. 102–113) and hence its more abrupt photodissociation. The "secondary" increase for H_2CO around 2×10^3 km may indicate an additional contribution from H_2CO released in the coma, as was first seen in Comet 1P/Halley from *Giotto* spacecraft Neutral Mass Spectrometer observations (Eberhardt 1999) and subsequently inferred from ground-based radio observations of C/1996B2 (Hyakutake; Biver et al. 1999) and C/1995 O1 (Hale-Bopp; Wink et al. 1999). Distributed emission of H_2CO was subsequently inferred in additional comets observed in the

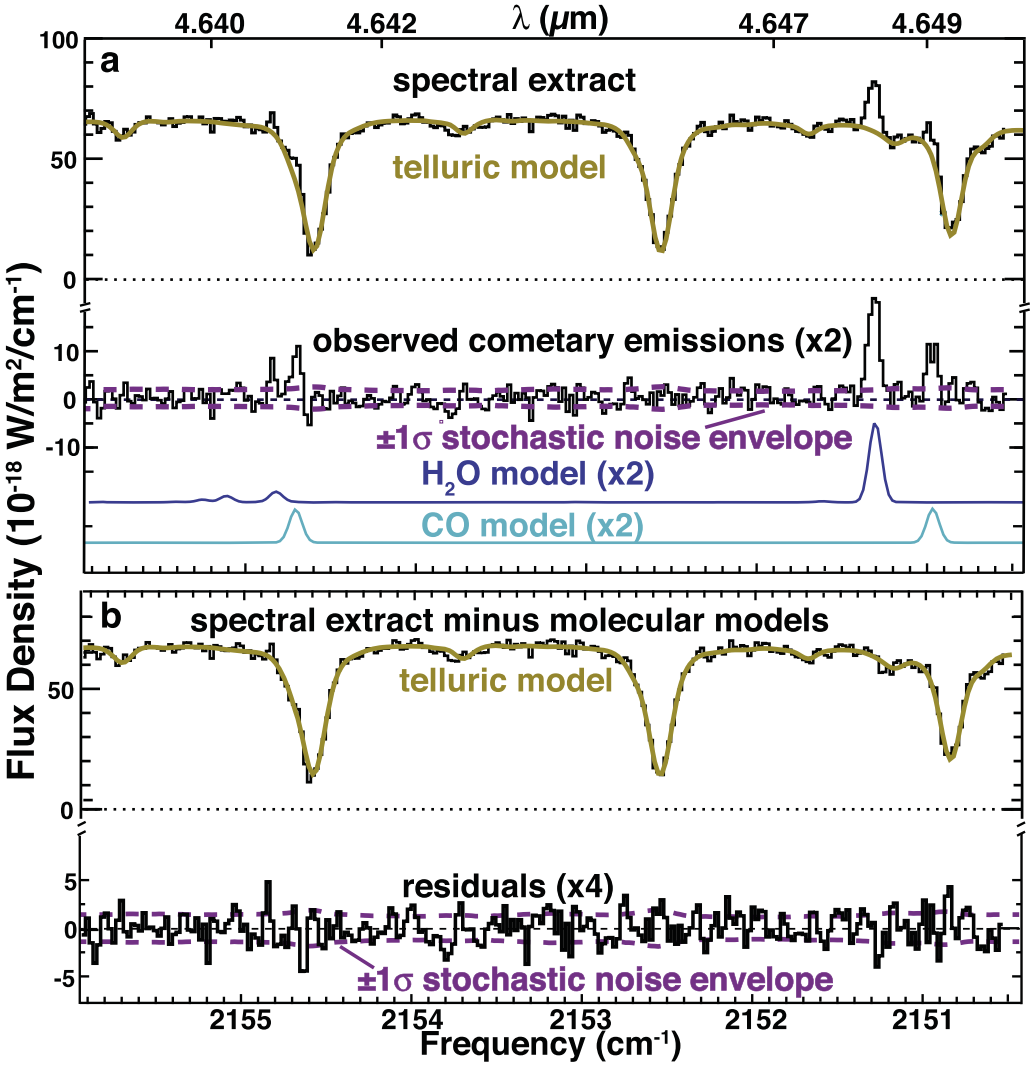

Figure 8. Graphical representation showing our iterative approach to quantifying terrestrial atmospheric absorption features and molecular production rates. The trace in panel (a) labeled "cometary emission" represents the *observed* net emission in excess of the continuum. For each spectral setting the goal is to accurately account for all features (telluric and cometary) such that the resulting "residual" spectrum (bottom trace in panel (b)) falls within the $\pm 1\sigma$ stochastic noise envelope (see Section 3.1 and Appendix A.1 for detailed discussions).

radio (Biver et al. 2002). ALMA observations of ISON on November 17.5 reported a symmetric and narrow spatial distribution of H_2CO, and significant contribution from a distributed source having a parent scale length of 230–330 km was suggested (Cordiner et al. 2014). Secondary increases are also suggested for HCN and H_2O (Figure 7), but at less pronounced levels. The secondary peaks for HCN, H_2O, and H_2CO occurred at somewhat differing offset distances, which could result from varying gas production over the nearly 2 hr of clock time encompassed by the three settings that measured these molecules on November 19.

Of the profiles shown in Figures 3 and 6, those of NH_3 are the most surprising. Although the photodissociation lifetime of ammonia is relatively short ($\tau_1 \sim 4 \times 10^3$ s; Huebner et al. 1992, pp. 169–177), Figures 6(c) and (e) show that its profile was very broad, comparable to or broader than that of the much longer-lived H_2O ($\tau_1 \sim 8 \times 10^4$ s) co-measured in the H2O_3C setting on both November 19 and 22. It also shows a dip in its central region that is present on both dates and is unique among spatial profiles we observed for Comet ISON, including continuum profiles. This either could result from optically thick pumping near the nucleus or alternatively could indicate release of NH_3 from a halo or shell of (ice- or grain-dominated) particles relatively close to (e.g., within a few hundred kilometers of) the nucleus. That is, its broad nature could indicate that a fraction of NH_3 was released in the coma, particularly if optical depth effects were unimportant. If optically thin, this result is highly surprising, since, unlike H_2CO, distributed release of NH_3 has not been reported for any comet.

When we applied the Q-curve formalism to co-measured NH_3 and H_2O profiles using their respective photodissociation lifetimes, the terminal region—which establishes $Q_{\rm tot}$ from measured molecular profiles (see Appendix A.3)—for H_2O was relatively level on both dates, as expected for release predominantly from the nucleus. However, in the case of NH_3, using its (considerably shorter) lifetime resulted in production rate values that continued to increase with ρ throughout the terminal region of the Q-curve. Leveling the terminal region for NH_3 required using a significantly longer effective lifetime, $\tau_1 \sim 2 \times 10^4$ s (or larger). This implies effective scale lengths of (at least) 5.0×10^3 and 3.3×10^3 km

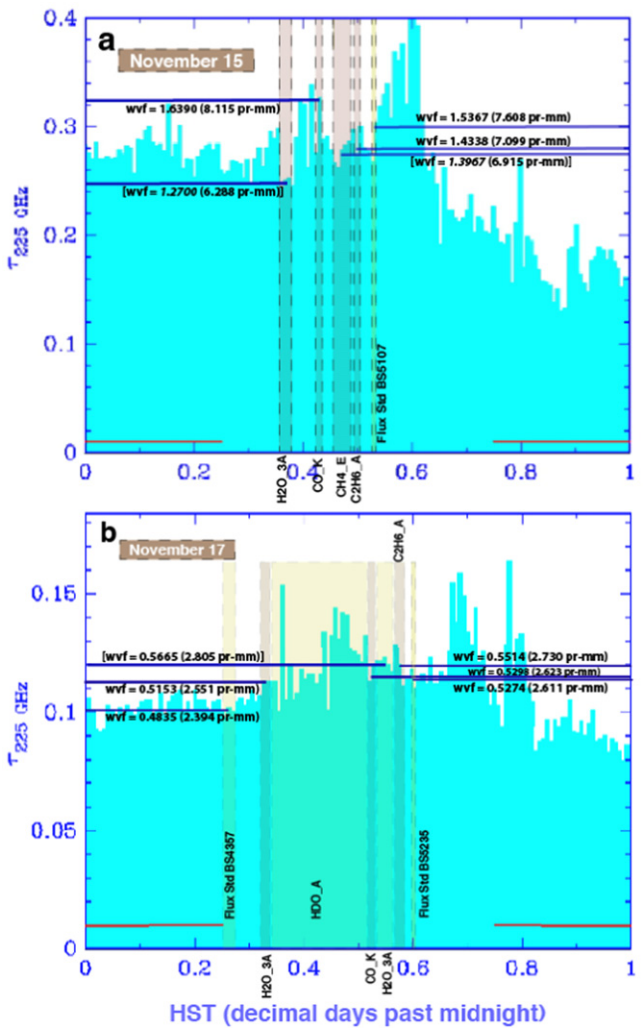

Figure 9. Sample CSO plots tracking the optical depth of H_2O absorption at 225 GHz on two 2013 dates, with CSHELL settings overplotted (shaded regions) according to the time spanned by each. "*HST*" on the *x*-axis denotes Hawaiian Standard Time (=UT – 10 hr).

for November 19 and 22, respectively, significantly larger than those expected for NH_3 assuming release solely from the nucleus ($\Lambda \sim 1.5 \times 10^3$ and 1.0×10^3 km for $R_h = 0.46$ and 0.35 AU, respectively).

A pronounced secondary peak for NH_3 occurred around $\rho = (1.8–2.0) \times 10^3$ km on November 19 and around 2.0×10^3 km on November 22, but on both dates these were displaced from the (relatively minor) secondary increases seen for *simultaneously measured* H_2O. Clearly, in addition to potential release in the coma, optical depth effects must be included in a detailed treatment of NH_3 emission in ISON for $R_h < 0.5$ AU.

The situation for HCN is also interesting. Did its higher abundance ratio inside 0.5 AU result from chemical heterogeneity in the nucleus, or was it dominated by release in the coma? If the latter, the scale for such release appears to be small, within the seeing profile.

In some comets the spatial distribution of HCN suggested the presence of (at least) two phases of ice within the nucleus, one dominated by polar and the other by apolar bonds (Mumma et al. 2011, 2014; Villanueva et al. 2011, 2012b; Paganini et al. 2012; DiSanti et al. 2014). In Comet ISON, no clear distinction between profiles of polar and apolar molecules was apparent.

Inspection of Figure 6(b) indicates that on November 19 the profile of NH_2 was similar to that of co-measured HCN. On November 22 this was also the case in the sunward-facing hemisphere; however, it more closely tracked the continuum profile antisunward. The extent to which the increase in NH_2 between 0.83 AU and within 0.5 AU tracks that of NH_3, the canonical candidate progenitor molecule of NH_2, requires detailed modeling of the outflow. This is outside the scope of our present study.

6. CONCLUSIONS

We report observations of Comet ISON on 10 UT dates between 2013 October 22 and November 22 (spanning $R_h = 1.213–0.344$ AU) using NIRSPEC at Keck II and CSHELL at the IRTF. Thirty-two measurements demonstrated that water production during this period varied by two orders of magnitude. Seven of these measurements were identified as likely being associated with reported "outburst" events. The remaining 25 measurements obeyed a heliocentric power law, $Q(H_2O) = (1.89 \pm 0.11) \times 10^{28} R_h^{(-3.10 \pm 0.09)}$ molecules s^{-1}, steeper than the canonical insolation-limited R_h^{-2} dependence and consistent with a factor of 50 increase in "baseline" water production in ISON.

We also obtained abundance ratios relative to H_2O for eight trace volatiles. Three of these (CO, C_2H_6, and CH_4) showed no systematic change in abundance with heliocentric distance, and they were depleted in ISON by factors of approximately 2–3 relative to their mean (or median) values found among comets, also referred to as their "current normal" abundances. CH_3OH showed somewhat more scatter, being depleted by a factor of ~2 for $R_h > 0.5$ AU but closer to its mean value for R_h within 0.5 AU.

Three other molecules (NH_3, H_2CO, and HCN) showed substantially increased abundance ratios within 0.5 AU of the Sun, while C_2H_2 showed a more modest increase. Outside $R_h = 0.5$ AU, the abundances of NH_3 and C_2H_2 were consistent with their current normal values, while H_2CO was depleted by 43% and HCN by 59%. Within 0.5 AU, all four of these molecules were enriched.

The column abundance of NH_2 relative to H_2O at $R_h = 0.83$ AU was slightly below the "typical" range found for NH/OH based on optical observations, but increased by factors of 3.3–6.1 inside of 0.5 AU. Detailed modeling is required to establish its production rate, to test whether its increase is consistent with that observed for NH_3, and also to test its release from photodissociation of NH_3 or other progenitor(s).

Surprisingly, the spatial distribution of NH_3 at $R_h = 0.46$ and 0.35 AU revealed a very broad profile, much more extended than expected were it released solely from the nucleus as optically thin emission. If optically thin, our analysis suggests that a substantial fraction of NH_3 was released by one or more progenitor species in the coma on a scale consistent with approximately 2×10^3 km from the nucleus. That of H_2CO was much less broad and suggested at most a modest contribution from distributed release at a similar distance from the nucleus.

This work was supported by Research Grant Awards through the NASA Planetary Atmospheres Program (PATM12-0049 to

M.A.D., and NNX12AG60G to B.P.B.), Planetary Astronomy Program (PAST11-0045 to M.J.M.), and the NSF Astronomy and Astrophysics Program (AST-1211362 to B.P.B. and E.L. G., and AST-1413736 to J.V.K.). This material is based in part on work supported by the National Aeronautics and Space Administration through the NASA Astrobiology Institute, issued through the Office of Space Science under grant 08NAI5-0005 to M.J.M., and under Cooperative Agreement Number NN09DA77A to K.J.M. We thank the Keck and IRTF for providing dedicated observing time for Comet ISON, and J. Green, K. Fast, and L. Johnson in the Planetary Science Division at NASA-HQ for their encouragement in supporting the overall ground- and space-based ISON observing campaign. We thank an anonymous referee for comments that improved the mauscript. M.A.D. gratefully acknowledges Strategic Science support from the Solar System Exploration Division at NASA-GSFC for his participation as a member of the Comet ISON Observing Campaign team. B.P.B.'s contribution to the Comet ISON Observing Campaign is dedicated to the memory of Hristo Hristov for his long distinguished service as a physics teacher in The Foreign Language School "Romain Rolland," Stara Zagora, Bulgaria. We recognize the very significant cultural role and reverence that the summit of Mauna Kea has always had within the indigenous Hawaiian community and feel most fortunate to conduct these observations from this mountain.

APPENDIX

A.1. Iterative Fitting of Telluric and Cometary Spectral Components

Figure 8 illustrates the approach we used for obtaining robust measures of absorbers in the telluric atmosphere and of molecular production rates in Comet ISON. We produced line spectra from processed spectral-spatial frames by summing signal over 3×9-pixels (0.43×1.78 arcsec) for NIRSPEC and over 5×15 pixels (1.0×3.0 arcsec) for CSHELL—in both cases these were centered on the peak emission intensity and represent the spatial apertures from which we calculated "nucleus-centered" production rates (see Section 3.2.2 and Table 2).

The atmospheric extinction (i.e., telluric transmittance) function (component 1 in Section 3.1) was first compared to the observed spectrum by omitting channels containing (known) strong cometary emission lines. This entailed convolving the fully resolved transmittance to the spectral resolving power of the data ($\mathrm{RP} \approx 2.5 \times 10^4$) and establishing approximate column burdens of absorbing species in the terrestrial atmosphere (Figure 8(a)).

Subtracting this convolved transmittance function (gold trace) from the spectral extract yields the observed cometary emissions in excess of the continuum (lower trace). These emissions are multiplied by the terrestrial transmittance function; to obtain actual emitted intensities requires dividing by the monochromatic atmospheric transmittance at each Doppler-shifted line position, as discussed in the literature (e.g., see Dello Russo et al. 1998; DiSanti et al. 2001; Villanueva et al. 2011).

The spectral resolving power and column burdens of telluric absorbers so obtained were then applied together with appropriate fluorescence models (Section 3.1, component 2) to establish initial nucleus-centered molecular production rates (Q_{nc}, Section 3.2.2). This was accomplished by fitting such models (H_2O and CO for the example shown; bottom traces in Figure 8(a)) to these cometary emissions. Our procedure is based on a Levenberg–Marquardt χ^2 minimization, developed previously for application to spectra of Mars's atmosphere (Villanueva et al. 2008).

Subtracting the fitted fluorescence models from the original spectral extract (top trace in Figure 8(a)) produces the top trace in Figure 8(b), which approximates the observed cometary dust continuum alone. The terrestrial transmittance function is then refit (i.e., RP and atmospheric absorber column burdens are reestablished), with the goal of producing overall residuals (bottom trace in Figure 8(b)) that are consistent with zero (i.e., that fall within the $\pm 1\sigma$ stochastic noise envelope). This telluric solution is then used to refit the fluorescence models as in Figure 8(a) and thereby obtain revised values for Q_{nc}. The process is repeated in an iterative manner between the steps depicted in Figures 8(a) and (b), and in most cases it converges within a few iterations. Telluric water burdens (precipitable millimeters, pr-mm) are included in Table 2 for all settings.

A.2. Comparing Telluric H_2O Fits with CSO Measurements

We compared the modeled telluric water burdens for our ISON spectra with concurrent Caltech Submillimeter Observatory (CSO) opacity measurements.[14] Figure 9 shows measured H_2O opacity at 225 GHz on two dates, upon which we superimpose the time intervals spanned by our CSHELL settings, identified by name below each panel and shown as rectangular shaded regions. For each setting, we indicate measured water vapor factor(s) (wvf) and corresponding pr-mm. This comparison was particularly important for those relatively few CSHELL settings in which the aforementioned iterative fitting process did not converge. In these cases we used the CSO measurements as a guide for approximating the telluric H_2O burden. Values estimated in this manner are shown in square brackets in Figure 9 and in parentheses in Table 2. (The weak [to absent] continuum in the NIRSPEC observations of Comet ISON required us to rely on standard star spectra in conjunction with concurrent CSO tau plots. For this reason, the corresponding pr-mm values applied to these observations are enclosed in parentheses in Table 2.) For all spectra this approach served to minimize the rms deviation in the residual spectrum, shown as the bottom trace and labeled "residuals" in Figure 8(b), and also in Figures 1 and 2.

A.3. Using Spatial Profiles of Emission to Determine Global Molecular Production Rates

Converting Q_{nc} to total (or global) production rate (Q_{tot}) requires accounting for flux lost, primarily owing to seeing, by virtue of using a narrow slit for both NIRSPEC and CSHELL observations. This involves applying a correction factor (a "growth factor"; GF in Table 2) established from measured spatial profiles of emission lines, such that $Q_{\mathrm{tot}} = Q_{\mathrm{nc}} \times \mathrm{GF}$. Our methodology is well documented in the literature; e.g., see Section 3.2 of DiSanti et al. (2014), Villanueva et al. (2011), Appendix B2 in Bonev et al. (2006), and Dello Russo et al. (1998) for detailed discussions of the "Q-curve" formalism.

[14] The relevant URL for these opacity measurements is cso.caltech.edu/tau/. The California Institute of Technology operated CSO, and archival tau measurements are available, up until its closure in 2015 September.

Spatial profiles of emissions from selected CSHELL observations of Comet ISON are shown in Figures 3 and 6. To establish GF, we use the mean signal from equidistant, diametrically opposite directions along the profile relative to the position of peak emission intensity, summing over multiple lines where possible. This averages over asymmetries in outflow and provides the most reliable measure of molecular production rates (see Xie & Mumma 1996 for details). In Table 2, retrieved values of Q_{nc}, measured (or assumed) GF, and Q_{tot} are listed by setting and by molecule, and for NIRSPEC observations, by echelle order.

The "Q-curve" formalism provides production rates that are relatively insensitive to the exact value of photodissociation lifetime (τ_1), as long as the scale length greatly exceeds the spatial coverage along the slit. The retrieval is more complicated for relatively short-lived species, in the present case most notably for H_2CO and NH_3 within $R_h = 0.5$ AU. Analysis of their spatial distributions suggests more complicated scenarios for their release (especially for NH_3) that may imply one or more additional sources in the coma, or alternatively optically thick conditions in the inner coma, as discussed in Section 5.2.

REFERENCES

Agúndez, M., Biver, N., Santos-Sanz, N., Bockelée-Morvan, D., & Moreno, R. 2014, A&A, 564, L2
A'Hearn, M. F., Millis, R. L., Schleicher, D. G., Osip, D. J., & Birch, P. V. 1995, Icar, 118, 223
Anderson, W. M. 2010, PhD thesis, The Catholic Univ. America
Biver, N., Agúndez, M., Santos-Sanz, P., et al. 2013, CBET, 3711, 2
Biver, N., Bockelée-Morvan, D., Colom, P., et al. 2011, A&A, 528, A142
Biver, N., Bockelée-Morvan, D., Crovisier, J., et al. 1999, AJ, 118, 1850
Biver, N., Bockelée-Morvan, D., Crovisier, J., et al. 2002, EM&P, 90, 323
Biver, N., Bockelée-Morvan, D., Lis, D. C., et al. 2006, A&A, 449, 1255
Bockelée-Morvan, D., Crovisier, J., Mumma, M. J., & Weaver, H. A. 2004, in Comets II, ed. M. C. Festou, H. U. Keller, & H. A. Weaver (Tucson, AZ: Univ. Arizona Press), 391
Boehnhardt, H. 2004, in Comets II, ed. M. C. Festou, H. U. Keller, & H. A. Weaver (Tucson, AZ: Univ. Arizona Press), 301
Boehnhardt, H., Tubiana, C., Oklay, N., & Vincent, J. B. 2013, CBET, 3715, 1
Bonev, B. P. 2005, PhD thesis, Univ. Toledo
Bonev, B. P., DiSanti, M. A., Villanueva, G. L., et al. 2014, ApJL, 796, L6
Bonev, B. P., Mumma, M. J., DiSanti, M. A., et al. 2006, ApJ, 653, 774
Bonev, B. P., Mumma, M. J., Gibb, E. L., et al. 2009, ApJ, 699, 1563
Clough, S. A., Shepherd, M. W., Mlawer, E. J., et al. 2005, JQSRT, 91, 233
Combi, M. R., Fougere, N., Mäkinen, J. T. T., et al. 2014, ApJL, 788, L7
Cordiner, M. A., Remijan, A. J., Boissier, J., et al. 2014, ApJL, 792, L2
Crovisier, J., Colom, P., Biver, N., & Bockelée-Morvan, D. 2013, CBET, 3711, 1
Dello Russo, N., DiSanti, M. A., Mumma, M. J., Magee-Sauer, K., & Rettig, T. W. 1998, Icar, 135, 377
Dello Russo, N., Vervack, R. J., Jr., Kawakita, H., et al. 2016, Icar, 266, 152
Dello Russo, N., Vervack, R. J., Jr., Weaver, H. A., et al. 2007, Natur, 448, 172
DiSanti, M. A., Anderson, W. M., Villanueva, G. L., et al. 2007, ApJL, 661, L101
DiSanti, M. A., Bonev, B. P., Magee-Sauer, K., et al. 2006, ApJ, 650, 470
DiSanti, M. A., & Mumma, M. J. 2008, SSRv, 138, 127
DiSanti, M. A., Mumma, M. J., Dello Russo, N., & Magee-Sauer, K. 2001, Icar, 153, 361
DiSanti, M. A., Villanueva, G. L., Paganini, L., et al. 2014, Icar, 228, 167
Eberhardt, P. 1999, SSRv, 90, 45
Faggi, S., Codella, C., Tozzi, G. P., et al. 2015, P&SS, 118, 173
Gibb, E. L., Bonev, B. P., DiSanti, M. A., et al. 2016, ApJ, in press
Gibb, E. L., Bonev, B. P., Villanueva, G. L., et al. 2012, ApJ, 750, 102
Gibb, E. L., DiSanti, M. A., Magee-Sauer, K., et al. 2007, Icar, 188, 224
Gibb, E. L., Whittet, D. C. B., Boogert, A. C. A., & Tielens, A. G. G. M. 2004, ApJS, 151, 35
Greene, T. P., Tokunaga, A. T., Toomey, D. W., & Carr, J. B. 1993, Proc. SPIE, 1946, 313
Hoban, S., Mumma, M. J., Reuter, D. C., & DiSanti, M. A. 1991, Icar, 93, 122
Huebner, W. F., Keady, J. J., & Lyon, S. P. 1992, Ap&SS, 195, 1
Knight, M. M., & Schleicher, D. G. 2015, AJ, 149, 19
Komitov, B., Shkodrov, V., Ivanova, V., & Stoyanova, S. 1989, AZh, 66, 1283
Levison, H. F., Duncan, M. J., Brasser, R., & Kaufmann, D. E. 2010, Sci, 329, 187
Magee-Sauer, K., Mumma, M. J., DiSanti, M. A., et al. 2008, Icar, 194, 347
McLean, I. S., Becklin, E. E., Bendiksen, O., et al. 1998, Proc. SPIE, 3354, 566
McLean, I. S., Graham, J. R., Becklin, E. E., et al. 2000, Proc. SPIE, 4008, 1048
Mumma, M. J., Bonev, B. P., Charnley, S. B., et al. 2014, BAAS, 46, 62
Mumma, M. J., Bonev, B. P., Villanueva, G. L., et al. 2011, ApJL, 734, L7
Mumma, M. J., & Charnley, S. B. 2011, ARA&A, 49, 471
Mumma, M. J., Dello Russo, N., DiSanti, M. A., et al. 2001, Sci, 292, 1334
Mumma, M. J., DiSanti, M. A., Magee-Sauer, K., et al. 2005, Sci, 310, 270
Mumma, M. J., DiSanti, M. A., Paganini, L., et al. 2013, IAUC, 9263, 2
Nevski, V., & Novichonok, A. 2012, CBET, 3238, 1
Öberg, K. I., Boogert, A. C. A., Pontoppidan, K. M., et al. 2011, ApJ, 740, 109
Opitom, C., Jehin, E., Manfroid, J., & Guillon, M. 2013a, CBET, 3711, 2
Opitom, C., Jehin, E., Manfroid, J., & Guillon, M. 2013b, CBET, 3719, 1
Paganini, L., Blake, G. A., Villanueva, G. L., et al. 2013, IAUC, 9263, 3
Paganini, L., Mumma, M. J., Villanueva, G. L., et al. 2012, ApJL, 748, L13
Paganini, L., Mumma, M. J., Villanueva, G. L., et al. 2014, ApJ, 791, 122
Radeva, Y. L., Mumma, M. J., Bonev, B. P., et al. 2010, Icar, 206, 764
Schmidt, C., Johnson, R. E., Baumgardner, J., & Mendillo, M. 2015, Icar, 247, 313
Sekanina, Z., & Kracht, R. 2014, arXiv:1404.5968v5
Tokunaga, A. T., Toomey, D. W., Carr, J., Hall, D. N. B., & Epps, H. W. 1990, Proc. SPIE, 1235, 131
Villanueva, G. L., Bonev, B. P., Mumma, M. J., et al. 2006, ApJL, 650, L87
Villanueva, G. L., DiSanti, M. A., Mumma, M. J., & Xu, L. H. 2012a, ApJ, 747, 37
Villanueva, G. L., Mumma, M. J., Bonev, B. P., et al. 2009, ApJL, 690, L5
Villanueva, G. L., Mumma, M. J., DiSanti, M. A., et al. 2011, Icar, 216, 227
Villanueva, G. L., Mumma, M. J., DiSanti, M. A., et al. 2012b, Icar, 220, 291
Villanueva, G. L., Mumma, M. J., Novak, R. E., & Hewagama, T. 2008, JQSRT, 109, 883
Weaver, H., Feldman, P., McCandliss, S., et al. 2013, CBET, 3680, 1
Wink, J., Bockelée-Morvan, D., Despois, D., et al. 1999, EM&P, 78, 63
Xie, X., & Mumma, M. J. 1996, ApJ, 464, 457
Yamamoto, T. 1982, A&A, 109, 326